Self-Heterodyne Diffractive Imaging of Ultrafast Electron Dynamics Monitored by Single-Electron Pulses

Shichao Sun (孙世超),[1,2] Haiwang Yong (雍海望),[1,2,*] Vladimir Y. Chernyak,[3,4,†] and Shaul Mukamel[1,2,‡]
[1]Department of Chemistry, University of California, Irvine, California 92614, USA
[2]Department of Physics and Astronomy, University of California, Irvine, California 92614, USA
[3]Department of Chemistry, Wayne State University, 5101 Cass Avenue, Detroit, Michigan 48202, USA
[4]Department of Mathematics, Wayne State University, 656 West Kirby, Detroit, Michigan 48202, USA

(Received 9 November 2023; revised 8 February 2024; accepted 18 July 2024; published 27 August 2024)

The direct imaging of time-evolving molecular charge densities on atomistic scale and at femtosecond resolution has long been an elusive task. In this theoretical study, we propose a self-heterodyne electron diffraction technique based on single electron pulses. The electron is split into two beams, one passes through the sample and its interference with the second beam produces a heterodyne diffraction signal that images the charge density. Application to probing the ultrafast electronic dynamics in Mg-phthalocyanine demonstrates its potential for imaging chemical dynamics.

DOI: 10.1103/PhysRevLett.133.093001

Ultrafast electron diffraction (UED) has been widely employed to probe molecular structural dynamics in space and time [1–12]. A pump optical laser pulse initiates an excited state dynamics and is followed by a probe electron pulse whose diffraction pattern reveals the time-evolving molecular charge density. The recent development of mega-electron-volt radio-frequency (rf) electron guns has enabled UED to monitor femtosecond molecular dynamics with atomistic spatial resolution [13–17]. Elaborate computational methods are required for retrieving the molecular charge density $\langle\hat{\sigma}(\boldsymbol{r})\rangle$ from UED signals. This is because standard homodyne detection gives the expectation values of products of charge-density operators $\langle\hat{\sigma}^{\dagger}\hat{\sigma}\rangle$,[18] while obtaining a real-space image requires the charge-density matrix itself in momentum space, including the phase, which goes beyond the expectation value of the charge density $\langle\hat{\sigma}\rangle$ alone [19]. Heterodyne-detected UED requires an additional reference wave that interferes with the scattered wave and can directly measure the time-evolving molecular charge density $\langle\sigma\rangle$ itself. It has been recently shown that the purely nuclear charge density can be singled out by subtracting the heterodyne x-ray scattering signal that images the electron density from heterodyne electron scattering signal [20,21]. Other diffraction and imaging techniques have been developed recently. Electron microscopies that utilize near field electron diffraction and homodyne detection can image the system with high space-time resolution [22,23]. Homodyne-detected x-ray diffraction probes the modulus square of electron charge density in momentum space [24,25]. Electron holography, a transmission electron microscopy method that records the interference of reference electron wave and an imaging wave, utilizes heterodyne-detected near field electron diffraction to image nanostructures [26–35]. Heterodyne-detected electron diffraction, as a far field electron diffraction, can achieve better spatial resolution down to picometer and can image the total electronic and nuclear charge density. However, the experimental implementation of heterodyne-detected UED remains a challenge.

Here, we introduce a novel self-heterodyned UED technique for imaging ultrafast molecular dynamics (Fig. 1), which employs a 1 fs single-electron pulse [36–40] followed by an electron biprism, which splits the beam into two [41–43]. The electron wave packet generated in one path interacts with the photo-excited molecular sample (signal path) and exchange momentum, while the other (reference path) traveling parallel to the signal path does not interact with the sample. A second electron biprism is finally used to combine the two paths, and the phase information of the scattered electron in the signal path can be reconstructed from the interference pattern. A detector monitors the electron and records the diffraction pattern, thereby measuring the interference of the two paths. The time-resolved signal is recorded by varying the time delay between optical pump pulse and single-electron probe pulse. In analogy to photon self-interference as explained by Dirac [44], the electron of the single-electron pulse interferes with itself. Since the relative phase of the two electron beam paths must be controlled in order to recover the phase of the signal, single-electron pulses that exclude

*Contact author: hyong@ucsd.edu
Present address: Department of Chemistry and Biochemistry, University of California San Diego, La Jolla, California 92093, USA.
†Contact author: chernyak@chem.wayne.edu
‡Contact author: smukamel@uci.edu

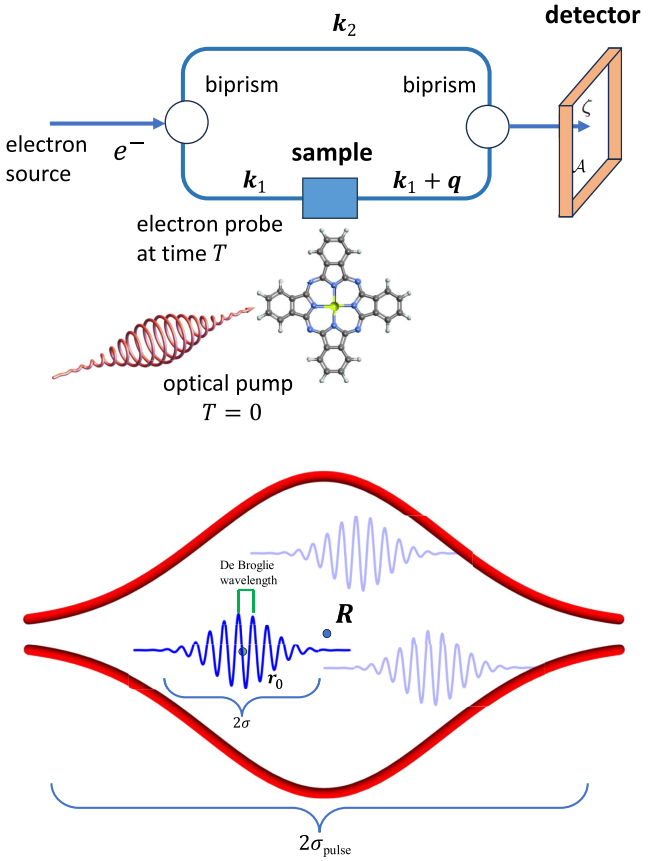

FIG. 1. Top: the self-heterodyned UED setup. The molecular sample is excited by an optical pump pulse at time 0. The electron source ejects a single electron, going through a biprism and separated into two replicas. One replica is scattered by the sample at time τ and changes its wave vector from $\mathbf{k}_1$ to $\mathbf{k}_1 + \mathbf{q}$. The other replica has wave vector $\mathbf{k}_2$. The two interfere at the detector. Bottom: the single electron pulse at the reference time t_0.

the interference of different electrons and remain coherent with themselves are most suitable for the proposed setup. In contrast, for multielectron pulses, when the beam electrons are incoherent, the interaction of incoherent electrons cannot recover the phase information. Besides the well-controlled phase information, single-electron pulses also overcome the space charge problem that limits the temporal duration of multielectron pulses [36–40,45]: due to Coulomb repulsion, multielectron pulses become longer during propagation from the source to the sample. Space charge is absent in pulses containing a single electron at a time. Femtosecond single-electron pulses with several keV electrons have been applied recently [46–48] to ultrafast microscopy and diffraction [45,49,50], demonstrating the feasibility of the proposed technique. Self-heterodyne diffraction can be alternatively performed with coherent multielectron pulses, where the pulse electrons remain coherent within the relevant spatiotemporal window [73,74], i.e., retain their phases. Measurements of electron diffraction with such multielectron pulses have improved data collection. However, multielectron pulses do not have the femtosecond temporal resolution required for measuring ultrafast electronic dynamics in molecular systems. Single-electron pulses are thus ideal for ensuring coherence of the electron beam and for ultrashort time resolution.

Heterodyne-detected diffraction can image the charge density on atomistic scale and with femtosecond time resolution. We demonstrate this by simulating this signal for Mg-phthalocyanine (MgPc) electronic dynamics with frozen nuclei. The signal probes the charge density temporal evolution in the current migration process, where the coherent ring currents created by an optical pump pulse redistribute among different locations within the MgPc molecule [75]. Similar to charge migration [76–84], current migration is caused by the time evolution of a coherent superposition of excited states.

In the proposed pump-probe setup, as illustrated in Fig. 1, an optical pump at time 0, first launches the electronic dynamics. The sample molecule excited by the optical pump pulse evolves according to the time-dependent Schrödinger equation

$$i\frac{\partial|\psi(t)\rangle}{\partial t} = [H_{\text{mol}} - \boldsymbol{\mu}\cdot\mathcal{E}(t)]|\psi(t)\rangle, \tag{1}$$

where $\mathcal{E}(t)$ is the optical pump electric field, $\psi(t)$ is the electronic wave function that may be expanded as $|\psi(t)\rangle = \sum_A c_A(t)|\psi_A\rangle$, and A runs over ground state and excited states. The charge-density operator in real space is given by

$$\hat{\sigma}(\boldsymbol{r}) = e\left(\sum_\alpha Z_\alpha \delta(\boldsymbol{r} - \boldsymbol{R}_\alpha) - \sum_i \delta(\boldsymbol{r} - \boldsymbol{r}_i)\right), \tag{2}$$

Here, Z_α and $\boldsymbol{R}_\alpha$ are nuclear charges and coordinates, α runs over the nuclei, $\boldsymbol{r}_i$ is the coordinate of electron i, and e is unit charge. The real-space charge density at time t is given by $\sigma(\boldsymbol{r}, t) = \langle\psi(t)|\hat{\sigma}(r)|\psi(t)\rangle$, or in momentum space,

$$\tilde{\sigma}(\boldsymbol{q}, t) = \int_{\mathbb{R}^3} d\boldsymbol{r} e^{-i\boldsymbol{q}\cdot\boldsymbol{r}}\sigma(\boldsymbol{r}, t). \tag{3}$$

The total time-dependent charge density can be decomposed as

$$\tilde{\sigma}(\boldsymbol{q}, t) = \sum_{A\in g\cup\text{ex}} \rho_{AA}(t)\tilde{\sigma}_{AA}(\boldsymbol{q}) + \sum_{A,B\in g\cup\text{ex}, A\neq B} \rho_{AB}(t)\tilde{\sigma}_{AB}(\boldsymbol{q}), \tag{4}$$

where A, B denote the electronic states, $\rho_{AB}(t) = c_A^*(t)c_B(t)$ is the density-matrix element. $\rho_{AA}(t)$ is the population of state A, while $\rho_{AB}(t)$ is the coherence between states A, B. The optical pump brings the system from the ground state to a superposition of excited states via the electric dipole interaction, Eq. (1). When the pump

pulse is over, the populations are stationary, while the electronic coherences ρ_{AB} oscillates with a period $[h/(E_A - E_B)]$, reflecting the difference of phase evolution of states A and B. The time-dependent charge density is thus solely attributed to electronic coherences.

The electron source ejects the probe electron, which is then split by an electron biprism into two beams. At a reference time t_0 before the probe electron interacts with the sample, the probe electron density matrix is $\rho_f(\boldsymbol{r}_1, \boldsymbol{r}_2; t_0)$ [or $\rho_{\boldsymbol{k}_1,\boldsymbol{k}_2}(t_0)$ in momentum space]. Starting at time t_0, the probe electron $\rho_{\boldsymbol{k}_1,\boldsymbol{k}_2}(t_0)$ propagates in the two beams. Electron beam 1 propagates according to the Coulomb potential created by the sample charge density,

$$u(\boldsymbol{r},\tau) = \int_{\mathbb{R}^3} d\boldsymbol{r}_\mu \frac{\langle \sigma(\boldsymbol{r}_\mu,\tau)\rangle}{|\boldsymbol{r}-\boldsymbol{r}_\mu|}, \qquad \tilde{u}(\boldsymbol{q},\tau) = 4\pi \frac{\langle \tilde{\sigma}(\boldsymbol{q},\tau)\rangle}{q^2}, \tag{5}$$

scatters off the sample at time τ, changing its wave vector from $\boldsymbol{k}_1$ to $\boldsymbol{k}_1 + \boldsymbol{q}$. Beam 2 propagates freely with a fixed wave vector $\boldsymbol{k}_2$. The magnitude distribution of the $\mathbf{k}_2$ is narrow, however its direction distribution should be wide enough to cover the range of $\boldsymbol{q}$. This interaction is described in Supplemental Material [50], Fig. S1. Treating the Coulomb potential Eq. (5) perturbatively, the probe electron density matrix at a later time t, $\rho_{\boldsymbol{k}_1+\boldsymbol{q},\boldsymbol{k}_2}(t)$ is calculated in Liouville space, as explained in Supplemental Material. Finally, the electron counting detector captures the probe electron from the two beams and measures the electron flux. Truncating the perturbative expansion of the density matrix to first order in the electron-sample interaction, we obtain the electron density matrix at time t, given as Eq. (S16) in Supplemental Material. By integrating the current density on surface $\mathcal{A}$ on the detector to calculate the electron flux, we obtain the expression for the electron diffraction signal at time t_D,

$$\mathcal{S}_0(\mathcal{A};\boldsymbol{q};t_D) = \frac{ie}{\hbar}\int_{t_0}^{\infty} d\tau \frac{\langle \tilde{\sigma}(\boldsymbol{q},\tau)\rangle}{\boldsymbol{q}^2} W_0(\mathcal{A};t_D,\boldsymbol{q},\tau) + \text{c.c.}, \tag{6}$$

where W_0 is the window function defined in Eq. (S22). Details of the window function are discussed in Sec. S2 of Supplemental Material.

The signal that reveals the time-dependent charge density in q space convoluted with the window function depends on the detection time t_D, the wave vector $\boldsymbol{q}$, and the detector area $\mathcal{A}$. Here, the single electron pulse diffraction signal is derived by neglecting the Coulombic interaction between the electrons in the pulse. This derivation also holds for multielectron pulses provided the number of electrons in the pulse is low and their Coulombic interaction can be neglected.

In the interaction of the probe electron and the sample, we neglected the contribution of inelastic scattering that involves vibrational state changes. We have also neglected the free-free transition where an electron passing close to an ion accelerates, and the laser assisted electron scattering where the probing electron is scattered by neutral matter in the process of laser, since the electron and the laser pulse have no temporal overlap in this proposed experiment.

The present self-heterodyne electron diffraction technique can be applied to single molecule or molecules aligned in periodic structure, preferably on a single layer of molecular film on lattice position, since the random orientation or position of molecules will make the self-heterodyne signal vanish. For a periodic sample, the diffraction signal Eq. (6) becomes a function of discrete value of $\boldsymbol{q} \in L_B$, where L_B is the periodic structure's corresponding Bragg lattice [Eqs. (S17),(S18)]. When the focal point of the electron beam is at the molecular location that only covers a single molecule, the measurement of a periodic system is equivalent to single molecule diffraction.

To obtain an analytical form for the window function, we assume that the probe electron has a Gaussian profile around the reference time t_0. The heterodyne electron diffraction of the single electron pulse should be measured repeatedly to accumulate enough signal strength for the detection of the diffraction pattern [39]. For each single electron pulse, the position of the Gaussian center $\boldsymbol{r}_0$ has a random variation [39]. We thus describe the probe electron as an ensemble of single electron pulses described by a mixed-state density matrix at time t_0,

$$\rho(\boldsymbol{r}_1,\boldsymbol{r}_2) = \frac{1}{\sqrt{2\pi}\sigma_{\text{pulse}}}\int d\boldsymbol{r}_0 \exp\left[-\frac{(\boldsymbol{r}_0-\boldsymbol{R})^2}{2\sigma_{\text{pulse}}^2}\right]\rho^{\text{pure}}(\boldsymbol{r}_1,\boldsymbol{r}_2). \tag{7}$$

This contains the pure state density matrix (ρ^{pure}) of Gaussian wave packet centered at $\boldsymbol{r}_0$, whose wave function in real space is

$$\phi(\boldsymbol{r}) = \frac{1}{\sqrt{2\pi}\sigma} e^{-i\boldsymbol{k}_0\cdot\boldsymbol{r}} \exp\left[-\frac{(\boldsymbol{r}-\boldsymbol{r}_0)^2}{2\sigma^2}\right], \tag{8}$$

while its center $\boldsymbol{r}_0$ is distributed around $\boldsymbol{R}$ with a Gaussian weight factor $\exp\left\{-[(\boldsymbol{r}_0-\boldsymbol{R})^2/2\sigma_{\text{pulse}}^2]\right\}$, as depicted in the lower panel of Fig. 1. Here, $\boldsymbol{k}_0$ is the average electron wave vector, σ denotes the spatial width of single electron at the reference time, σ_{pulse} is the width of the Gaussian wave center $\boldsymbol{r}_0$ distribution. We use the same width in the longitudinal and transverse directions. We further used an electron average energy of $E_0 = 100$ keV, $|\boldsymbol{k}_0| = 85.7\ (\hbar/a_0)$, where a_0 is Bohr radius, c is the speed of light and m_0 is electron mass. Its De Broglie wavelength 3.88 pm, determines the spatial resolution, i.e., the upper

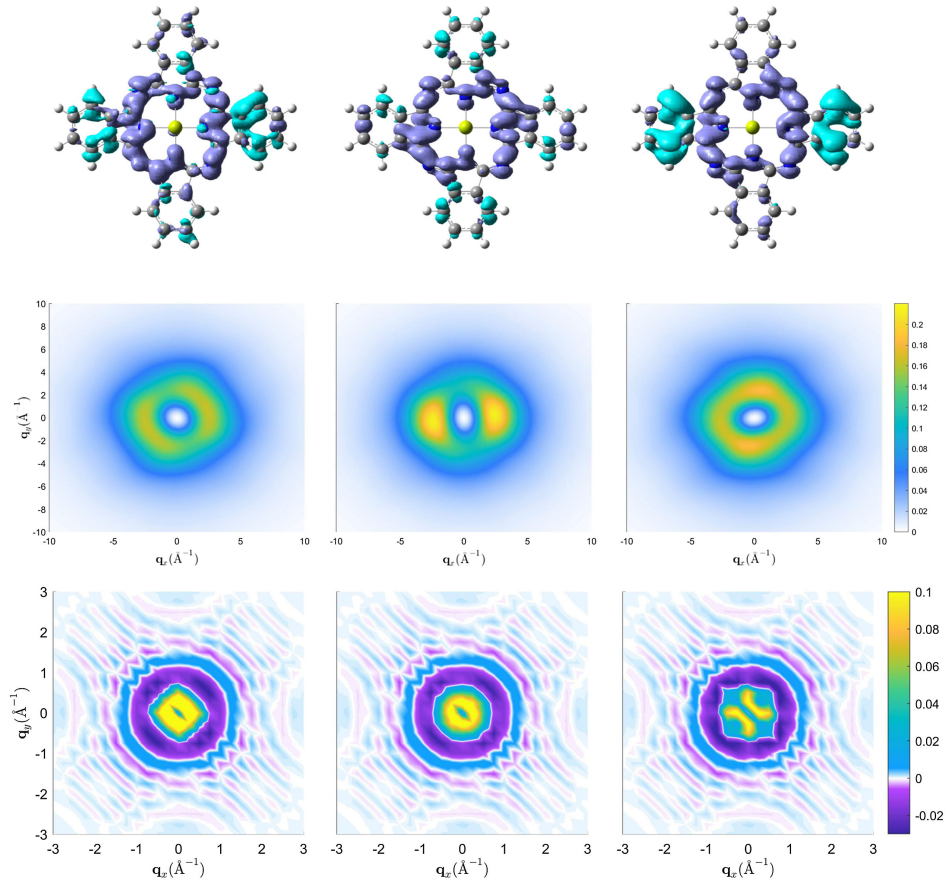

FIG. 2. Top row: real space charge density at time τ minus the charge density at the initial time step, $[\sigma(\mathbf{r},\tau)-\sigma(\mathbf{r},-3.9\text{ fs})]$. Second row: the real part of charge density in q-space, $(\Re[\tilde{\sigma}(\mathbf{q},\tau)-\tilde{\sigma}(\mathbf{q},-3.9\text{ fs})])$. Analytical integral Eq. (3) is evaluated with the algorithm of Ref. [92]. Third row: the diffraction signal $[\mathcal{S}_0'(\mathbf{q};t_D)-\mathcal{S}_0'(\mathbf{q};-3.9\text{ fs})]$. The first, second, and third columns are at times 2.1 fs, 8.1 fs, 17.1 fs, respectively.

limit of $|\boldsymbol{q}|$ in the diffraction pattern. $\boldsymbol{R}$ is set at the origin, while $\sigma = 22.066$ Å, $\sigma_{\text{pulse}} = 1103.3$ Å. The probe pulse duration 1.18 fs is the pulse length ($2\sigma_{\text{pulse}}$) divided by electron velocity. The electron coherence time is given by its coherence length (2σ) divided by its velocity, 0.047 fs. The window function is Eq. (S42) in Supplemental Material. Using Eq. (6), we define the signal as

$$\mathcal{S}_0'(\boldsymbol{q},\mathcal{A};t_D) = \boldsymbol{q}^2\mathcal{S}_0(\boldsymbol{q},\mathcal{A};t_D). \tag{9}$$

We have applied this technique to probe the electronic dynamics in Mg-phthalocyanine (MgPc) initiated by a circularly polarized light pump pulse. Details of the dynamics are discussed in Supplemental Material and in Refs. [50,75]. Phthalocyanines have many applications in, e.g., dye-sensitized solar cells [85,86] and as photosensitizers for cancer photodynamic therapy [87]. MgPc has a rigid structure, which remains stable upon electronic excitation [88,89]. It is a planar molecule consisting of a center porphyrin ring and four corner benzene rings (see Fig. 1). Its high density of excited states in the 2 to 4 eV regime, facilitates the coherent excitation of multiple excited states by a broadband pump pulse [75]. The circularly polarized pump drives the electron in the conjugated π bond moving in a circle, resulting in ring currents proportional to the electronic state coherence, $\boldsymbol{j}(t) = \sum_{A,B,A\neq B}\rho_{AB}\boldsymbol{j}_{AB}$, where $\boldsymbol{j}_{AB}$ is transition current density, analogous to the coherent charge density in Eq. (4). These coherent ring currents vary with time due to the superposition of multiple electronic states. Since different coherent currents have distinct spatial profiles, some concentrated in the central ring while others reside in the corner rings, the ring currents redistribute among different regions of the molecule with time, resulting in a current migration process between the central and the corner rings [75]. Similar to current migration, the interplay of coherent charge-density oscillations induced by multiple pairs of coherences causes the dynamics of charge density, i.e., the charge density redistributes among the central porphyrin and the corner benzene rings, as depicted in the first row of Fig. 2 and Fig. S2 in Supplemental Material. The charge density is more pronounced on the central ring and left and right rings, and moves to the top and bottom

rings, and back. Such change can also be reflected in the real part of q-space charge density (second row of Fig. 2) and the diffraction pattern (third row of Fig. 2). Although electron diffraction does not directly image the current density, it images the charge density, originating from the same electronic coherence ρ_{AB}. However, the continuity relation $-(\partial\rho/\partial t) = \boldsymbol{\nabla}\cdot\boldsymbol{j}$ connects the time evolution of the charge density to the divergence of the current density [90,91].

Figures S2 and S5 display the charge density in real space and the diffraction pattern of the system prior to the pump pulse where no current density exists. First row of Fig. 2 depicts the charge-density difference $[\sigma(\boldsymbol{r},\tau) - \sigma(\boldsymbol{r}, -3.9\text{ fs})]$, where the charge density at time -3.9 fs before the pump is subtracted from the charge density at time τ. The second row displays the charge density difference in q-space $\tilde{\sigma}(\boldsymbol{q},\tau) - \tilde{\sigma}(\boldsymbol{q}, -3.9\text{ fs})$, while the third row depicts the diffraction signal difference $\mathcal{S}_0'(\boldsymbol{q},\mathcal{A};t_D) - \mathcal{S}_0'(\boldsymbol{q},\mathcal{A};-3.9\text{ fs})$. The diffraction signal is simulated by convoluting the charge density and the instrumental window function. The window function has both real and imaginary parts. Once integrated over the charge density, both parts contribute to the diffraction pattern. The real (imaginary) part of the charge density is an even (odd) function of $\boldsymbol{q}$ [see Eq. (3)]. We find that the resulting diffraction pattern is dominated by the stronger real part.

During the optical pump, the excited state population ρ_{AA} increases, inducing a population ring current [75,93] and charge density [first term in Eq. (4)]. Since the electronic state population is time-independent once the pump pulse is over, the time dependence of the signal after the optical pump pulse only comes from electronic coherences. If the pump has a narrow bandwidth that only covers one pair of excited state and one coherent ring current like in Refs. [93–95], the corresponding coherent ring current and coherent charge density oscillate with the coherence, i.e., the coherent current density reverses direction while the coherent charge density changes sign at the frequency of coherence. For a broad band pump, the superposition of multiple pairs of coherence causes current migration and a redistribution of charge density among different regions of the molecule, as seen in the diffraction signal Fig. 2 and Supplemental Material Fig. S5. The electronic dynamics involves excited states of irreducible representation E_u. Since E_u in D_{4h} point group has character -2 with respect to inversion, the charge-density change is symmetric for inversion. For this reason, the charge-density change of the electronic dynamics in real space has a central symmetry. The diffraction signal integrates the window function and the momentum-space charge density. The real (imaginary) part of $\tilde{\sigma}(\boldsymbol{q},\tau)$ is central symmetric (antisymmetric). The resulting diffraction pattern has central symmetry, as the real part of window function dominates. The diffraction signal changes mostly occur within -2 to 2 Å^{-1}, since the window function decays rapidly for larger $|\boldsymbol{q}|$. The diffraction signal is thus only clear when the scattering wave vector $|\boldsymbol{q}|$ is smaller than some threshold. To measure the signal in a broader range of $\boldsymbol{q}$, higher energy single-electron pulses should be employed.

In a future study, we will apply relativistic theory for describing higher energy probing electrons and simulating their self-heterodyne diffraction signal. Reconstruction of the real-space charge density from the diffraction signal requires the inverse Fourier transform of the three-dimensional momentum-space charge density $\tilde{\sigma}(\boldsymbol{q},\tau)$. The diffraction signal integrates the window function with $\tilde{\sigma}(\boldsymbol{q},\tau)$, thus mixing its real and imaginary parts. Obtaining $\tilde{\sigma}(\boldsymbol{q},\tau)$ requires: (1) measuring the diffraction signal at various q_z; (2) performing phase-shifting [43,96–98] measurement, i.e., varying the relative phase of the signal and reference electron beam to separately obtain real and imaginary parts of the complex valued function; (3) deconvoluting the window function.

In summary, we have proposed a self-heterodyne electron diffraction method for imaging the molecular charge density in real time and space. A single probe electron is split into two beams, where only one travels through the sample. The diffraction signal is obtained by the interference of these two paths. This ultrafast imaging of the charge density in q space can monitor electron dynamics in real time. It is demonstrated by simulating the time-resolved signal of MgPc electronic dynamics initiated by a UV-visible circularly polarized light pulse. The proposed technique is not limited to probing electronic dynamics like current and charge migration, but can be also applied to the imaging of various light-induced ultrafast chemical processes.

Acknowledgments—V. Y. C. gratefully acknowledges the support of the US Department of Energy, Office of Science, Basic Energy Sciences Award No. DESC0022134. S. S. was supported by the National Science Foundation through Grant No. CHE-2246379. S. M. was supported by the U.S. Department of Energy, Office of Science, Office of Basic Energy Sciences under Award No. DE-FG02-04ER15571.

[1] A. H. Zewail, 4d ultrafast electron diffraction, crystallography, and microscopy, Annu. Rev. Phys. Chem. **57**, 65 (2006).

[2] W. E. King, G. H. Campbell, A. Frank, B. Reed, J. F. Schmerge, B. J. Siwick, B. C. Stuart, and P. M. Weber, Ultrafast electron microscopy in materials science, biology, and chemistry, J. Appl. Phys. **97**, 111101 (2005).

[3] C. J. Hensley, J. Yang, and M. Centurion, Imaging of isolated molecules with ultrafast electron pulses, Phys. Rev. Lett. **109**, 133202 (2012).

[4] J. Yang, J. Beck, C. J. Uiterwaal, and M. Centurion, Imaging of alignment and structural changes of carbon disulfide molecules using ultrafast electron diffraction, Nat. Commun. **6**, 8172 (2015).

[5] A. A. Ischenko, P. M. Weber, and R. D. Miller, Capturing chemistry in action with electrons: Realization of atomically resolved reaction dynamics, Chem. Rev. **117**, 11066 (2017).
[6] J. Yang *et al.*, Imaging cf_3i conical intersection and photodissociation dynamics with ultrafast electron diffraction, Science **361**, 64 (2018).
[7] Y. Xiong, K. J. Wilkin, and M. Centurion, High-resolution movies of molecular rotational dynamics captured with ultrafast electron diffraction, Phys. Rev. Res. **2**, 043064 (2020).
[8] J. Yang, X. Zhu, J. P. F. Nunes, J. K. Yu, R. M. Parrish, T. J. A. Wolf, M. Centurion, M. Gühr, R. Li, Y. Liu, B. Moore, M. Niebuhr, S. Park, X. Shen, S. Weathersby, T. Weinacht, T. J. Martinez, and X. Wang, Simultaneous observation of nuclear and electronic dynamics by ultrafast electron diffraction, Science **368**, 885 (2020).
[9] K. J. Wilkin, Y. Xiong, H. Zhao, S. B. Muvva, S. K. Saha, and M. Centurion, Ultrafast electron diffraction from transiently aligned asymmetric top molecules: Rotational dynamics and structure retrieval, Struct. Dyn. **9**, 054303 (2022).
[10] D. Filippetto, P. Musumeci, R. K. Li, B. J. Siwick, M. R. Otto, M. Centurion, and J. P. F. Nunes, Ultrafast electron diffraction: Visualizing dynamic states of matter, Rev. Mod. Phys. **94**, 045004 (2022).
[11] Y. Wang, S. K. Saha, T. Li, Y. Xiong, K. Wilkin, A. Adhikari, M. Loes, J. Abourahma, X. Hong, S. Adenwalla, A. Sinitskii, and M. Centurion, Ultrafast electron diffraction instrument for gas and condensed matter samples, Rev. Sci. Instrum. **94**, 053001 (2023).
[12] E. G. Champenois *et al.*, Femtosecond electronic and hydrogen structural dynamics in ammonia imaged with ultrafast electron diffraction, Phys. Rev. Lett. **131**, 143001 (2023).
[13] J. B. Hastings, F. M. Rudakov, D. H. Dowell, J. F. Schmerge, J. D. Cardoza, J. M. Castro, S. M. Gierman, H. Loos, and P. M. Weber, Ultrafast time-resolved electron diffraction with megavolt electron beams, Appl. Phys. Lett. **89**, 184109 (2006).
[14] H.-C. Shao and A. F. Starace, Imaging coherent electronic motion in atoms by ultrafast electron diffraction, Phys. Rev. A **88**, 062711 (2013).
[15] J. Yang *et al.*, Femtosecond gas phase electron diffraction with MeV electrons, Faraday Discuss. **194**, 563 (2016).
[16] X. Shen, J. P. F. Nunes, J. Yang, R. K. Jobe, R. K. Li, M.-F. Lin, B. Moore, M. Niebuhr, S. P. Weathersby, T. J. A. Wolf, C. Yoneda, M. Guehr, M. Centurion, and X. J. Wang, Femtosecond gas-phase mega-electron-volt ultrafast electron diffraction, Struct. Dyn. **6**, 054305 (2019).
[17] M. Centurion, T. J. Wolf, and J. Yang, Ultrafast imaging of molecules with electron diffraction, Annu. Rev. Phys. Chem. **73**, 21 (2022).
[18] J. R. Rouxel, D. Keefer, and S. Mukamel, Signatures of electronic and nuclear coherences in ultrafast molecular X-ray and electron diffraction, Struct. Dyn. **8**, 014101 (2021).
[19] K. Bennett, M. Kowalewski, J. R. Rouxel, and S. Mukamel, Monitoring molecular nonadiabatic dynamics with femtosecond X-ray diffraction, Proc. Natl. Acad. Sci. U.S.A. **115**, 6538 (2018).
[20] H. Yong, D. Keefer, and S. Mukamel, Imaging purely nuclear quantum dynamics in molecules by combined X-ray and electron diffraction, J. Am. Chem. Soc. **144**, 7796 (2022).
[21] H. Yong, D. Keefer, and S. Mukamel, Novel ultrafast molecular imaging based on the combination of X-ray and electron diffraction, J. Phys. Chem. A **127**, 835 (2023).
[22] Y. Morimoto and P. Baum, Diffraction and microscopy with attosecond electron pulse trains, Nat. Phys. **14**, 252 (2018).
[23] J. H. Gaida, H. Lourenço-Martins, M. Sivis, T. Rittmann, A. Feist, F. J. García de Abajo, and C. Ropers, Attosecond electron microscopy by free-electron homodyne detection, Nat. Photonics **18**, 509 (2024).
[24] H. J. Suominen and A. Kirrander, How to observe coherent electron dynamics directly, Phys. Rev. Lett. **112**, 043002 (2014).
[25] V. S. Yakovlev, M. I. Stockman, F. Krausz, and P. Baum, Atomic-scale diffractive imaging of sub-cycle electron dynamics in condensed matter, Sci. Rep. **5**, 14581 (2015).
[26] K. Harada, Interference and interferometry in electron holography, Microscopy **70**, 3 (2021).
[27] H. Lichte and M. Lehmann, Electron holography—basics and applications, Rep. Prog. Phys. **71**, 016102 (2007).
[28] D. Gabor, A new microscopi prinnciple, Nature (London) **161**, 777 (1948).
[29] D. Gabor and W. L. Bragg, Microscopy by reconstructed wave-fronts, Proc. R. Soc. A **197**, 454 (1949).
[30] R. E. Dunin-Borkowski, A. Kovács, T. Kasama, M. R. McCartney, and D. J. Smith, Electron holography, in *Springer Handbook of Microscopy*, edited by P. W. Hawkes and J. C. H. Spence (Springer International Publishing, Cham, 2019), pp. 767–818.
[31] F. Houdellier, G. M. Caruso, S. Weber, M. Hÿtch, C. Gatel, and A. Arbouet, Optimization of off-axis electron holography performed with femtosecond electron pulses, Ultramicroscopy **202**, 26 (2019).
[32] H. Lichte, Electron holography approaching atomic resolution, Ultramicroscopy **20**, 293 (1986).
[33] A. Tonomura, T. Matsuda, J. Endo, T. Arii, and K. Mihama, Direct observation of fine structure of magnetic domain walls by electron holography, Phys. Rev. Lett. **44**, 1430 (1980).
[34] A. Tonomura, Applications of electron holography, Rev. Mod. Phys. **59**, 639 (1987).
[35] H. Lichte, Electron holography: Phases matter, Microscopy **62**, S17 (2013).
[36] B. J. Siwick, J. R. Dwyer, R. E. Jordan, and R. D. Miller, Ultrafast electron optics: Propagation dynamics of femtosecond electron packets, J. Appl. Phys. **92**, 1643 (2002).
[37] S. Collin, M. Merano, M. Gatri, S. Sonderegger, P. Renucci, J.-D. Ganière, and B. Deveaud, Transverse and longitudinal space-charge-induced broadenings of ultrafast electron packets, J. Appl. Phys. **98** (2005).
[38] A. Gliserin, A. Apolonski, F. Krausz, and P. Baum, Compression of single-electron pulses with a microwave cavity, New J. Phys. **14**, 073055 (2012).
[39] P. Baum, On the physics of ultrashort single-electron pulses for time-resolved microscopy and diffraction, Chem. Phys. **423**, 55 (2013).

[40] S. Tsesses, R. Dahan, K. Wang, T. Bucher, K. Cohen, O. Reinhardt, G. Bartal, and I. Kaminer, Tunable photon-induced spatial modulation of free electrons, Nat. Mater. **22**, 345 (2023).
[41] G. Möllenstedt and H. Düker, Fresnelscher interferenzversuch mit einem biprisma für elektronenwellen, Naturwissenschaften **42**, 41 (1955).
[42] K. Harada, H. Endoh, and R. Shimizu, Anti-contamination electron biprism for electron holography, J. Electron Microsc. **37**, 199 (1988).
[43] Z. Chen, B. Zhang, Y. Pan, and M. Krüger, Quantum wave function reconstruction by free-electron spectral shearing interferometry, Sci. Adv. **9**, eadg8516 (2023).
[44] P. A. M. Dirac, *The Principles of Quantum Mechanics* (Oxford University Press, New York, 1981) "Each photon then interferes only with itself. Interference between two different photons never occurs".
[45] M. Hassan, Electron microscopy for attosecond science, Phys. Today **77**, No. 6, 38 (2024).
[46] B. Barwick, D. J. Flannigan, and A. H. Zewail, Photon-induced near-field electron microscopy, Nature (London) **462**, 902 (2009).
[47] L. Kasmi, D. Kreier, M. Bradler, E. Riedle, and P. Baum, Femtosecond single-electron pulses generated by two-photon photoemission close to the work function, New J. Phys. **17**, 033008 (2015).
[48] L. Waldecker, R. Bertoni, and R. Ernstorfer, Compact femtosecond electron diffractometer with 100 keV electron bunches approaching the single-electron pulse duration limit, J. Appl. Phys. **117** (2015).
[49] S. Asban, D. Keefer, V. Y. Chernyak, and S. Mukamel, Sensing ultrashort electronic coherent beating at conical intersections by single-electron pulses, Proc. Natl. Acad. Sci. U.S.A. **119**, e2205510119 (2022).
[50] See Supplemental Material at http://link.aps.org/supplemental/10.1103/PhysRevLett.133.093001, which includes Refs. [46–48,51–66], for comparison of photon-induced near field electron microscopy with self-heterodyne electron diffraction and includes [67–72], for the density functional theory and time-dependent density functional theory simulation details.
[51] F. G. de Abajo and M. Kociak, Electron energy-gain spectroscopy, New J. Phys. **10**, 073035 (2008).
[52] F. J. García de Abajo, A. Asenjo-Garcia, and M. Kociak, Multiphoton absorption and emission by interaction of swift electrons with evanescent light fields, Nano Lett. **10**, 1859 (2010).
[53] A. Howie, Photon interactions for electron microscopy applications, Euro. Phys. J.-Appl. Phys. **54**, 33502 (2011).
[54] M. Aidelsburger, F. O. Kirchner, F. Krausz, and P. Baum, Single-electron pulses for ultrafast diffraction, Proc. Natl. Acad. Sci. U.S.A. **107**, 19714 (2010).
[55] S. T. Park, M. Lin, and A. H. Zewail, Photon-induced near-field electron microscopy (PINEM): Theoretical and experimental, New J. Phys. **12**, 123028 (2010).
[56] S. T. Park and A. H. Zewail, Photon-induced near field electron microscopy, in *Ultrafast Imaging and Spectroscopy*, Vol. 8845, edited by Z. Liu, International Society for Optics and Photonics (SPIE, 2013), p. 884506, 10.1117/12.2023082.
[57] S. T. Park and A. H. Zewail, Photon-induced near-field electron microscopy: Mathematical formulation of the relation between the experimental observables and the optically driven charge density of nanoparticles, Phys. Rev. A **89**, 013851 (2014).
[58] S. T. Park and A. H. Zewail, Relativistic effects in photon-induced near field electron microscopy, J. Phys. Chem. A **116**, 11128 (2012).
[59] M. T. Hassan, Attomicroscopy: From femtosecond to attosecond electron microscopy, J. Phys. B **51**, 032005 (2018).
[60] Y. Pan, B. Zhang, and A. Gover, Anomalous photon-induced near-field electron microscopy, Phys. Rev. Lett. **122**, 183204 (2019).
[61] K. Wang, R. Dahan, M. Shentcis, Y. Kauffmann, A. Ben Hayun, O. Reinhardt, S. Tsesses, and I. Kaminer, Coherent interaction between free electrons and a photonic cavity, Nature (London) **582**, 50 (2020).
[62] O. Reinhardt and I. Kaminer, Theory of shaping electron wavepackets with light, ACS Photonics **7**, 2859 (2020).
[63] Y. Kurman, R. Dahan, H. H. Sheinfux, K. Wang, M. Yannai, Y. Adiv, O. Reinhardt, L. H. G. Tizei, S. Y. Woo, J. Li, J. H. Edgar, M. Kociak, F. H. L. Koppens, and I. Kaminer, Spatiotemporal imaging of 2d polariton wave packet dynamics using free electrons, Science **372**, 1181 (2021).
[64] D. J. Flannigan, B. Barwick, and A. H. Zewail, Biological imaging with 4d ultrafast electron microscopy, Proc. Natl. Acad. Sci. U.S.A. **107**, 9933 (2010).
[65] M. Kaplan, B.-K. Yoo, J. Tang, T. E. Karam, B. Liao, D. Majumdar, D. Baltimore, G. J. Jensen, and A. H. Zewail, Photon-induced near-field electron microscopy of eukaryotic cells, Angew. Chem. **129**, 11656 (2017).
[66] X. Fu, Z. Sun, S. Ji, F. Liu, M. Feng, B.-K. Yoo, and Y. Zhu, Nanoscale-femtosecond imaging of evanescent surface plasmons on silver film by photon-induced near-field electron microscopy, Nano Lett. **22**, 2009 (2022).
[67] A. D. Becke, Density-functional exchange-energy approximation with correct asymptotic behavior, Phys. Rev. A **38**, 3098 (1988).
[68] A. D. Becke, Density-functional thermochemistry. III. The role of exact exchange, J. Chem. Phys. **98**, 5648 (1993).
[69] C. Lee, W. Yang, and R. G. Parr, Development of the Colle-Salvetti correlation-energy formula into a functional of the electron density, Phys. Rev. B **37**, 785 (1988).
[70] B. Miehlich, A. Savin, H. Stoll, and H. Preuss, Results obtained with the correlation energy density functionals of becke and Lee, Yang and Parr, Chem. Phys. Lett. **157**, 200 (1989).
[71] M. J. Frisch *et al.*, Gaussian 16 Revision A.03, Gaussian Inc., Wallingford, CT, 2016.
[72] D. B. Williams-Young, A. Petrone, S. Sun, T. F. Stetina, P. Lestrange, C. E. Hoyer, D. R. Nascimento, L. Koulias, A. Wildman, J. Kasper, J. J. Goings, F. Ding, A. E. DePrince III, E. F. Valeev, and X. Li, The Chronus Quantum (ChronusQ) Software Package, WIREs Comput. Mol. Sci. **10**, e1436 (2020).
[73] T. Kodama, N. Osakabe, and A. Tonomura, Correlation in a coherent electron beam, Phys. Rev. A **83**, 063616 (2011).
[74] D. Ehberger, J. Hammer, M. Eisele, M. Krüger, J. Noe, A. Högele, and P. Hommelhoff, Highly coherent electron beam

from a laser-triggered tungsten needle tip, Phys. Rev. Lett. **114**, 227601 (2015).
[75] S. Sun, H. Yong, F. Chen, and S. Mukamel, Coherent ring-current migration of mg-phthalocyanine probed by time-resolved X-ray circular dichroism, Chem. Sci. **13**, 10327 (2022).
[76] M. F. Kling and M. J. Vrakking, Attosecond electron dynamics, Annu. Rev. Phys. Chem. **59**, 463 (2008).
[77] M. Nisoli, P. Decleva, F. Calegari, A. Palacios, and F. Martín, Attosecond electron dynamics in molecules, Chem. Rev. **117**, 10760 (2017).
[78] H. J. Wörner, C. A. Arrell, N. Banerji, A. Cannizzo, M. Chergui, A. K. Das, P. Hamm, U. Keller, P. M. Kraus, E. Liberatore *et al.*, Charge migration and charge transfer in molecular systems, Struct. Dyn. **4**, 061508 (2017).
[79] L. S. Cederbaum and J. Zobeley, Ultrafast charge migration by electron correlation, Chem. Phys. Lett. **307**, 205 (1999).
[80] A. I. Kuleff, J. Breidbach, and L. S. Cederbaum, Multi-electron wave-packet propagation: General theory and application, J. Chem. Phys. **123**, 044111 (2005).
[81] A. J. Jenkins, M. Vacher, R. M. Twidale, M. J. Bearpark, and M. A. Robb, Charge migration in polycyclic norbornadiene cations: Winning the race against decoherence, J. Chem. Phys. **145**, 164103 (2016).
[82] F. Mauger, P. M. Abanador, A. Bruner, A. Sissay, M. B. Gaarde, K. Lopata, and K. J. Schafer, Signature of charge migration in modulations of double ionization, Phys. Rev. A **97**, 043407 (2018).
[83] A. S. Folorunso, A. Bruner, F. Mauger, K. A. Hamer, S. Hernandez, R. R. Jones, L. F. DiMauro, M. B. Gaarde, K. J. Schafer, and K. Lopata, Molecular modes of attosecond charge migration, Phys. Rev. Lett. **126**, 133002 (2021).
[84] Y. Kobayashi, D. M. Neumark, and S. R. Leone, Theoretical analysis of the role of complex transition dipole phase in XUV transient-absorption probing of charge migration, Opt. Express **30**, 5673 (2022).
[85] M. G. Walter, A. B. Rudine, and C. C. Wamser, Porphyrins and phthalocyanines in solar photovoltaic cells, J. Porphyrins Phthalocyanines **14**, 759 (2010).
[86] M. Urbani, M.-E. Ragoussi, M. K. Nazeeruddin, and T. Torres, Phthalocyanines for dye-sensitized solar cells, Coord. Chem. Rev. **381**, 1 (2019).
[87] Z. Jiang, J. Shao, T. Yang, J. Wang, and L. Jia, Pharmaceutical development, composition and quantitative analysis of phthalocyanine as the photosensitizer for cancer photodynamic therapy, J. Pharm. Biomed. Anal. **87**, 98 (2014).
[88] J. Mi, L. Guo, Y. Liu, W. Liu, G. You, and S. Qian, Excited-state dynamics of magnesium phthalocyanine thin film, Phys. Lett. A **310**, 486 (2003).
[89] D. Potamianos, M. Nuber, A. Schletter, M. Schnitzenbaumer, M. Haimerl, P. Scigalla, M. Wörle, L. I. Wagner, R. Kienberger, and H. Iglev, Full dynamics description of Mg phthalocyanine crystalline and amorphous semiconductor systems, J. Phys. Chem. C **125**, 18279 (2021).
[90] A. Moreno Carrascosa, M. Yang, H. Yong, L. Ma, A. Kirrander, P. M. Weber, and K. Lopata, Mapping static core-holes and ring-currents with X-ray scattering, Faraday Discuss. **228**, 60 (2021).
[91] G. Hermann, V. Pohl, G. Dixit, and J. C. Tremblay, Probing electronic fluxes via time-resolved X-ray scattering, Phys. Rev. Lett. **124**, 013002 (2020).
[92] S. Sun, D. Williams-Young, T. F. Stetina, and X. Li, Generalized Hartree-Fock with non-perturbative treatment of strong magnetic field: Application to molecular spin phase transition, J. Chem. Theory Comput. **15**, 348 (2019).
[93] I. Barth, J. Manz, Y. Shigeta, and K. Yagi, Unidirectional electronic ring current driven by a few cycle circularly polarized laser pulse: Quantum model simulations for Mg- porphyrin, J. Am. Chem. Soc. **128**, 7043 (2006).
[94] I. Barth and J. Manz, Periodic electron circulation induced by circularly polarized laser pulses: Quantum model simulations for Mg porphyrin, Angew. Chem. Int. Ed. **45**, 2962 (2006).
[95] Y. Nam, J. R. Rouxel, J. Y. Lee, and S. Mukamel, Monitoring aromatic ring-currents in Mg-porphyrin by time-resolved circular dichroism, Phys. Chem. Chem. Phys. **22**, 26605 (2020).
[96] I. Yamaguchi and T. Zhang, Phase-shifting digital holography, Opt. Lett. **22**, 1268 (1997).
[97] T. Zhang and I. Yamaguchi, Three-dimensional microscopy with phase-shifting digital holography, Opt. Lett. **23**, 1221 (1998).
[98] I. Yamaguchi, Phase-shifting digital holography, in *Digital Holography and Three-Dimensional Display: Principles and Applications*, edited by T.-C. Poon (Springer US, Boston, MA, 2006), pp. 145–171.

Supplementary Information: Self-heterodyne Diffractive Imaging of Ultrafast Molecular Dynamics Monitored by Single-Electron Pulses

Shichao Sun (孙世超)[a,b], Haiwang Yong (雍海望)[a,b,*] Vladimir Y. Chernyak[d,e,†] and Shaul Mukamel[a,b‡]
[a] Department of Chemistry, University of California, Irvine, CA 92614, USA
[b] Department of Physics and Astronomy, University of California, Irvine, CA 92614, USA
[c] Department of Chemistry and Biochemistry, University of California San Diego, La Jolla, CA 92093, USA
[d] Department of Chemistry, Wayne State University,
5101 Cass Ave, Detroit, Michigan 48202, USA and
[e] Department of Mathematics, Wayne State University, 656 W. Kirby, Detroit, Michigan 48202, USA
(Dated: June 5, 2024)

S1. SELF-HETERODYNE ELECTRON SPECTROSCOPY SIGNAL: DERIVATION DETAILS

In the present study, an optical source creates a driving optical field, induce the photoionization process in the electron reservoir (like a piece of normal metal) and eject high energy probe electrons. On the other hand, another optical field drives the sample molecule out of its equilibrium state and initiate electron dynamics.

In our case we have electrons in a sample under study, as well as in a subsystem, e.g., a piece of normal metal, referred to as the reservoir, that serves as a source for the probe electrons. We should also introduce a sources, responsible for the optical fields that drives the sample out of its equilibrium state, as well as an optical source creating a driving optical field, responsible for the photoionization processes, thus creating high-energy probe electrons. A source is represented by its time-dependent charge/current densities $(\rho(\boldsymbol{r},t),\boldsymbol{j}(\boldsymbol{r},t))$ that satisfy the continuity equation $\partial_t\rho+\operatorname{div}\boldsymbol{j}=0$, the latter ensuring gauge invariance of the interaction of the source with the scalar and vector potentials.

We further introduce the following simplifications/approximations. Since the sample, reservoir, and probe electrons are well separated either in real space, or energy-momentum space, we will describe them using three independent quantum fields. The Hamiltonion of the entire system can therefore be represented in a form

$$H(t)=H_0(t)+H^{\rm int}(t),\quad H_0(t)=H_\mu(t)+H_f+H_s,\quad H^{\rm int}(t)=H_\mu^{\rm int}+H_s^{\rm int}(t). \tag{S1}$$

In Eq. (S1), $H_0(t)$ includes the kinetic and Coulomb energy $H_\mu(t)$ of the charged particles (electrons and nuclei) in the sample, the energy H_f of the free transverse electromagnetic field (photons), the coupling H_s of the photons to the charged particles of the sample, as well as to the optical source, responsible to the sample driving field, as prescribed by QED; its time dependence originates from the optical source-photon couplig. H_f and H_s represent the Hamiltonians of free probe electrons and the reservoir electrons respectively; $H_\mu^{\rm int}$ represents Coulomb interactions between the probe and sample electrons, as well as the coupling between the probe electrons and photons. Finally, $H_s^{\rm int}(t)$ describes photoionization processes which convert the reservoir electrons to fast probe counterparts; this is a simplified description of photoinization, compared to the original QED treatment that uses an optical source of the photoinization field, coupled to the source and free electrons via transverse photons, obtained by invoking a classical approximation for the photoionizing field. The initial density matrix of the whole system is assumed to be in a factorized form

$$\varrho=\varrho_\mu\otimes\varrho_f\otimes\varrho_{\rm s}, \tag{S2}$$

with ϱ_μ representing the canonical distribution of the material/sample (including photons) at some actual temperature T, ϱ_f represents a pure state with no electrons, while ϱ_s is an equilibrium state of the electron reservoir. A more detailed derivation of Eq. (S1), based on the effective action formalism, will be published elsewhere.

Neglecting the probe electron scattering on the sample excitations via a transverse photon exchange, i.e., limiting it to pure Coulomb, we have

$$H_\mu^{int}=\int d\boldsymbol{r}d\boldsymbol{r}'\frac{\sigma_\mu(\boldsymbol{r}')\sigma_f(\boldsymbol{r})}{|\boldsymbol{r}-\boldsymbol{r}'|},\quad \sigma_f(\boldsymbol{r})=-e\Psi^\dagger(\boldsymbol{r})\Psi(\boldsymbol{r}), \tag{S3}$$

* hyong@ucsd.edu; Present address: Department of Chemistry and Biochemistry, University of California San Diego, La Jolla, CA 92093, USA
† chernyak@chem.wayne.edu
‡ smukamel@uci.edu

where $\sigma_\mu(\boldsymbol{r})$ is the charge density operator, associated with the sample, whereas $\Psi(\boldsymbol{r})$ and $\Psi^\dagger(\boldsymbol{r})$ are the probe electron annihilation and creation operators, respectively. The reservoir-probe electron coupling Hamitonian can be represented as

$$H_s^{int}(t) = \int d\boldsymbol{r}(\Psi^\dagger(\boldsymbol{r})\Theta(\boldsymbol{r},t) + \Theta^\dagger(\boldsymbol{r},t)\Psi(\boldsymbol{r})), \tag{S4}$$

where $\Theta(\boldsymbol{r},t)$ and $\Theta^\dagger(\boldsymbol{r},t)$ are time-dependent operators that represent collective reservoir variables, their time-dependence originates from the time dependence of the ionizing field.

Hereafter we use the following standard convention: for a Hilbert space operator Q, we denote Q_α, with $\alpha = \mathrm{L}, \mathrm{R}, \pm$, the corresponding Liouville space operators, $Q_\alpha(t)$ is the Heisenberg (time-dependent) counterpart of Q_α with respect to Liouville space dynamics, associated with the Liouville operator $\mathcal{L} = H_-$, whereas $\tilde{Q}_\alpha(t)$ is the Heisenberg operator, associated with the Liouville operator $\mathcal{L}_0 = (H_0)_-$. It is convenient to consider the most general signal, associated with counting the total number of beam electrons in the detector; it has a very simple form in terms of the Liouville-space correlation functions of the beam electron variables

$$\mathcal{S}(\boldsymbol{r},t;\boldsymbol{r}',t')) = \langle \Psi_{\mathrm{L}}(\boldsymbol{r},t)\Psi^\dagger_{\mathrm{R}}(\boldsymbol{r}',t')\rangle = \mathrm{Tr}(\mathrm{T}(\Psi_{\mathrm{L}}(\boldsymbol{r},t)\Psi^\dagger_{\mathrm{R}}(\boldsymbol{r}',t'))(\varrho)), \quad \mathcal{S}(\boldsymbol{r},\boldsymbol{r}';t)) = \mathcal{S}(\boldsymbol{r},t;\boldsymbol{r}',t)) \tag{S5}$$

where T denotes Liouville space chronological time ordering, and the time dependence of the operators in Eq. (S5) is determined by the Heisenberg picture/formalism, as per the convention, described above. To perform a perturbative expansion, we recast Eq. (S5) in the interaction picture, treating H^{int} in Eq. (S1) as a perturbation to H_0

$$\mathcal{S}(\boldsymbol{r},t;\boldsymbol{r}',t')) = \left\langle \tilde{\Psi}_{\mathrm{L}}(\boldsymbol{r},t)\tilde{\Psi}^\dagger_{\mathrm{R}}(\boldsymbol{r}',t')\exp\left(-i\hbar^{-1}\int d\tau \tilde{H}^{int}_-(\tau)\right)\right\rangle. \tag{S6}$$

Note that, by definition of the Liouville space correlation functions, the operators inside the angular brackets in Eq. (S6) should be chronologically time-ordered, so that when expanding the exponential term in a Taylor series, one can disregard the non-commutative nature of operators. Since interaction between the sample/material system and the beam electrons is weak, due to the high energy of the free electrons, and the density of the beam electrons is low, we will look at the lowest orders of perturbation theory that provide a non-vanishing signal, which is first order in H^{int}_μ and second order in H^{int}_s [or, in Liouville space, it boils down to first order in $H^{int}_{s,\mathrm{L}}$ and first order in $H^{int}_{s,\mathrm{R}}$], the signal is linear in the density of beam electrons, so that their Coulomb interaction can be neglected.

To obtain a closed formal expression for the signal, we note that within the above approximations, the expression in the r.h.s. of Eq. (S6) contains one of each of the operators $\tilde{\sigma}_\mu$, Θ_{L}, and Θ_{R} and 6 probe electron operators (3 creation plus 3 annihilation). Computing the 6-point Liouville space correlation function of the probe electrons by applying the Liouville space variant of the Wick theorem[1], we obtain

$$\begin{aligned}\mathcal{S}(\boldsymbol{r},\boldsymbol{r}';t)) = &-\left(\frac{1}{\hbar}\right)^3 \int_{\mathbb{R}^3} d\tau d\tau_1 d\tau_2 \int_{X^{\times 3}} d\boldsymbol{r}_f d\boldsymbol{r}_1 d\boldsymbol{r}_2 u(\boldsymbol{r}_f,\tau) \\ &G(\boldsymbol{r},\boldsymbol{r}_f,t-\tau)G(\boldsymbol{r}_f,\boldsymbol{r}_1,\tau-\tau_1)(G(\boldsymbol{r}',\boldsymbol{r}_2,t-\tau_2))^* K(\boldsymbol{r}_1,\tau_1,\boldsymbol{r}_2,\tau_2) + \text{c.c.},\end{aligned} \tag{S7}$$

where

$$u(\boldsymbol{r}_f,t) = \int d\boldsymbol{r}_\mu \frac{\langle\tilde{\sigma}_\mu(\boldsymbol{r}_\mu,t)\rangle}{|\boldsymbol{r}-\boldsymbol{r}_\mu|}, \tag{S8}$$

is the Coulomb potential, associated with the photo-induced charge density in the sample, whereas G and K are the retarded correlation functions of the probe beam electrons and the "population" correlation function of the reservoir collective variables, respectively:

$$G(\boldsymbol{r},\boldsymbol{r}';t-t') = -i\langle\tilde{\Psi}_{\mathrm{L}}(\boldsymbol{r},t)\tilde{\Psi}^\dagger_{\mathrm{L}}(\boldsymbol{r}',t')\rangle, \quad K(\boldsymbol{r},t;\boldsymbol{r}',t') = \langle\tilde{\Theta}_{\mathrm{L}}(\boldsymbol{r},t)\tilde{\Theta}^\dagger_{\mathrm{R}}(\boldsymbol{r}',t')\rangle. \tag{S9}$$

Note that $G(\boldsymbol{r},\boldsymbol{r}';t) = 0$ for $t < 0$, and $K(\boldsymbol{r},t;\boldsymbol{r}',t')$ completely describes the beam of high-energy probe electrons, and plays a role of some kind of dynamical spectral density of the high-energy electron source. In what follows, we will use the following expression for the retarded correlation function of the probe electrons

$$G(\boldsymbol{r},\boldsymbol{r}';t) = -i\chi_{\mathbb{R}_+}(t)\int_{\mathbb{R}^3}\frac{d\boldsymbol{k}}{(2\pi)^3}e^{i\boldsymbol{k}\cdot(\boldsymbol{r}-\boldsymbol{r}')}e^{-i\varepsilon_{\boldsymbol{k}}t}, \quad \varepsilon_{\boldsymbol{k}} = \frac{\hbar\boldsymbol{k}^2}{2m}, \quad \chi_{\mathbb{R}_+}(t) = \frac{1}{2}(1+\mathrm{sgn}\,(t)). \tag{S10}$$

where sgn is the sign function, $\mathrm{sgn}\,(t) = \begin{cases}1, & \text{if}\, t>0\\ 0, & \text{if}\, t=0,\\ -1, & \text{if}\, t<0.\end{cases}$. Eq. (S7) can be further simplified under the reasonable assumption that the electron reservoir is located far away from the experimental sample, so that there is a moment

in time t_0, the ionizing pulse is gone [i.e., $H_s^{int}(t) = 0$, for $t > t_0$], whereas the probe electron wavepacket is still far enough from the sample, so that we can set $H_\mu^{int}(t) = 0$, for $t < t_0$. This allows the time integration in Eq. (S7) to be restricted to $\tau_1, \tau_2 \in (-\infty, t_0)$ and $\tau \in (t_0, t)$. Since the retarded Green function $G(\boldsymbol{r}, \boldsymbol{r}'; t)$ represents the kernel of the one-electron evolution operator, it possesses the time concatenation property, allowing Eq. (S7) to be recast in a simpler form

$$\begin{aligned}
&\mathcal{S}(\boldsymbol{r}, \boldsymbol{r}'; t) = \frac{1}{\hbar}\int_{t_0}^{t} d\tau \int_{X^{\times 3}} d\boldsymbol{r}_f d\boldsymbol{r}_1 d\boldsymbol{r}_2 u(\boldsymbol{r}_f, \tau) \\
&G(\boldsymbol{r}, \boldsymbol{r}_f, t-\tau) G(\boldsymbol{r}_f, \boldsymbol{r}_1, \tau - t_0)(G(\boldsymbol{r}', \boldsymbol{r}_2, t-t_0))^* \rho_f(\boldsymbol{r}_1, \boldsymbol{r}_2; t_0) + \text{c.c.}, \\
&\rho_f(\boldsymbol{r}_1, \boldsymbol{r}_2; t_0) = \left(\frac{1}{\hbar}\right)^2 \int_{-\infty}^{t_0} d\tau_1 \int_{-\infty}^{t_0} d\tau_2 G(\boldsymbol{r}_1, \boldsymbol{r}_1'; t_0 - \tau_1)(G(\boldsymbol{r}_2, \boldsymbol{r}_2'; t_0 - \tau_2))^* K(\boldsymbol{r}_1', \tau_1, \boldsymbol{r}_2', \tau_2).
\end{aligned} \tag{S11}$$

where $\rho_f(\boldsymbol{r}_1, \boldsymbol{r}_2; t_0)$ should be viewed as a reduced one-electron density of the probe electron beam at time t_0, which represents all relevant properties of the probe electron source, in application to the considered signal in the lowest non-vanishing perturbative order described above. Note that the relevant properties of the probe electron source are generally described by a one-elctron mixed state, rather than a pure state.

Eqs. (S11), and (S8) together with Eq. (S10) constitute a complete set of integral expressions for the signal considered in this paper. They clearly demostrate that the dynamical information that can be retrieved from the considered spectroscopic measurement is the time- and position-dpendent charge density, induced in the experimental setup upon photoexcitation.

The expression for the signal $S(\boldsymbol{r}, \boldsymbol{r}'; t, t')$ can be further simplified by introducing the Fourier transform of the Coulomb interaction, induced charge density and the probe electron reduced density matrix,

$$u(\boldsymbol{r}_f, \tau) = \int_{\mathbb{R}^3} \frac{d\boldsymbol{q}}{(2\pi)^3} e^{i\boldsymbol{q}\cdot\boldsymbol{r}_f} \tilde{u}(\boldsymbol{q}, \tau) = 4\pi \int_{\mathbb{R}^3} \frac{d\boldsymbol{q}}{(2\pi)^3} e^{i\boldsymbol{q}\cdot\boldsymbol{r}_f} \frac{\sigma_\mu(\boldsymbol{q}, \tau)}{\boldsymbol{q}^2}, \tag{S12}$$

$$\langle \tilde{\sigma}_\mu(\boldsymbol{r}, \tau)\rangle = \int_{\mathbb{R}^3} \frac{d\boldsymbol{q}}{(2\pi)^3} e^{i\boldsymbol{q}\cdot\boldsymbol{r}} \sigma_\mu(\boldsymbol{q}, \tau), \tag{S13}$$

and

$$\rho_f(\boldsymbol{r}_1, \boldsymbol{r}_2; t_0) = \int_{\mathbb{R}^3} \frac{d\boldsymbol{k_1}}{(2\pi)^3} \int_{\mathbb{R}^3} \frac{d\boldsymbol{k_2}}{(2\pi)^3} e^{i\boldsymbol{k}_1\cdot\boldsymbol{r}_1 - i\boldsymbol{k}_2\cdot\boldsymbol{r}_2} \rho_{\boldsymbol{k}_1, \boldsymbol{k}_2}(t_0), \tag{S14}$$

and substituting Eq. (S12), Eqs. (S13) and (S14), together with the integral representation for the one-electron Green functions Eq. (S10) into Eq. (S11).

$$\begin{aligned}
\mathcal{S}(\boldsymbol{r}, \boldsymbol{r}'; t) =& \frac{1}{\hbar}\int_{t_0}^{t} d\tau \int_{X^{\times 3}} d\boldsymbol{r}_f d\boldsymbol{r}_1 d\boldsymbol{r}_2 u(\boldsymbol{r}_f, \tau) G(\boldsymbol{r}, \boldsymbol{r}_f, t-\tau) G(\boldsymbol{r}_f, \boldsymbol{r}_1, \tau - t_0)(G(\boldsymbol{r}', \boldsymbol{r}_2, t-t_0))^* \rho_f(\boldsymbol{r}_1, \boldsymbol{r}_2; t_0) + \text{c.c.} \\
=& 4\pi \frac{1}{\hbar}\int_{t_0}^{t} d\tau \int_{\mathbb{R}^3} d\boldsymbol{r}_f \int_{\mathbb{R}^3} \frac{d\boldsymbol{q}}{(2\pi)^3} e^{i\boldsymbol{q}\cdot\boldsymbol{r}_f} \frac{\sigma_\mu(\boldsymbol{q}, \tau)}{\boldsymbol{q}^2} \int_{X^{\times 2}} d\boldsymbol{r}_1 d\boldsymbol{r}_2 \int_{\mathbb{R}^3} \frac{d\boldsymbol{k_1}}{(2\pi)^3} \int_{\mathbb{R}^3} \frac{d\boldsymbol{k_2}}{(2\pi)^3} e^{i\boldsymbol{k}_1\cdot\boldsymbol{r}_1 - i\boldsymbol{k}_2\cdot\boldsymbol{r}_2} \rho_{\boldsymbol{k}_1, \boldsymbol{k}_2}(t_0) \\
&\times \big(-i\chi_{\mathbb{R}_+}(t-\tau)\big) \int_{\mathbb{R}^3} \frac{d\boldsymbol{k}_3'}{(2\pi)^3} e^{i\boldsymbol{k}_3'\cdot(\boldsymbol{r}-\boldsymbol{r}_f)} e^{-i\varepsilon_{\boldsymbol{k}_3'}(t-\tau)} \big(-i\chi_{\mathbb{R}_+}(\tau - t_0)\big) \int_{\mathbb{R}^3} \frac{d\boldsymbol{k}_1'}{(2\pi)^3} e^{i\boldsymbol{k}_1'\cdot(\boldsymbol{r}_f-\boldsymbol{r}_1)} e^{-i\varepsilon_{\boldsymbol{k}_1'}(\tau-t_0)} \\
&\times \big(i\chi_{\mathbb{R}_+}(t-t_0)\big) \int_{\mathbb{R}^3} \frac{d\boldsymbol{k}_2'}{(2\pi)^3} e^{-i\boldsymbol{k}_2'\cdot(\boldsymbol{r}'-\boldsymbol{r}_2)} e^{i\varepsilon_{\boldsymbol{k}_2'}(t-t_0)} + \text{c.c.} \\
=& 4\pi \frac{1}{\hbar}\int_{t_0}^{t} d\tau \int_{\mathbb{R}^3} \frac{d\boldsymbol{q}}{(2\pi)^3} \frac{\sigma_\mu(\boldsymbol{q}, \tau)}{\boldsymbol{q}^2} \int_{\mathbb{R}^3} \frac{d\boldsymbol{k_1}}{(2\pi)^3} \int_{\mathbb{R}^3} \frac{d\boldsymbol{k_2}}{(2\pi)^3} \rho_{\boldsymbol{k}_1, \boldsymbol{k}_2}(t_0) \\
&\times \big(-i\chi_{\mathbb{R}_+}(t-\tau)\big)\big(-i\chi_{\mathbb{R}_+}(\tau - t_0)\big)\big(i\chi_{\mathbb{R}_+}(t-t_0)\big) \\
&\times \int_{\mathbb{R}^3} \frac{d\boldsymbol{k}_1'}{(2\pi)^3} \int_{\mathbb{R}^3} \frac{d\boldsymbol{k}_2'}{(2\pi)^3} \int_{\mathbb{R}^3} \frac{d\boldsymbol{k}_3'}{(2\pi)^3} e^{i\varepsilon_{\boldsymbol{k}_2'}(t-t_0)} e^{-i\varepsilon_{\boldsymbol{k}_1'}(\tau-t_0)} e^{-i\varepsilon_{\boldsymbol{k}_3'}(t-\tau)} e^{i\boldsymbol{k}_3'\cdot\boldsymbol{r}} e^{-i\boldsymbol{k}_2'\cdot\boldsymbol{r}'} \\
&\times \delta(\boldsymbol{k}_3' - \boldsymbol{q} - \boldsymbol{k}_1')\delta(\boldsymbol{k}_1' - \boldsymbol{k}_1)\delta(\boldsymbol{k}_2' - \boldsymbol{k}_2) + \text{c.c.}
\end{aligned} \tag{S15}$$

where the spatial integrations of $\boldsymbol{r}_1, \boldsymbol{r}_2, \boldsymbol{r}_f$ is performed, resulting in the δ-functions, that reflect momentum conservation for all scattering processes involved. Performing the integration of $\boldsymbol{k}_1', \boldsymbol{k}_2', \boldsymbol{k}_3'$, we have the expression

$$S(\boldsymbol{r},\boldsymbol{r}';t,t') = \frac{ie}{\hbar}\int_{t_0}^{t} d\tau \int_{\mathbb{R}^3} \frac{d\boldsymbol{q}}{(2\pi)^3}\frac{\sigma_\mu(\boldsymbol{q},\tau)}{\boldsymbol{q}^2}\int_{\mathbb{R}^3}\frac{d\boldsymbol{k}_1}{(2\pi)^3}\int_{\mathbb{R}^3}\frac{d\boldsymbol{k}_2}{(2\pi)^3}\rho_{\boldsymbol{k}_1,\boldsymbol{k}_2}(t_0)e^{i[(\boldsymbol{k}_1+\boldsymbol{q})\cdot\boldsymbol{r}-i\boldsymbol{k}_2\cdot\boldsymbol{r}']} \times e^{-i\varepsilon_{\boldsymbol{k}_1}(\tau-t_0)-i\varepsilon_{\boldsymbol{k}_1+\boldsymbol{q}}(t-\tau)+i\varepsilon_{\boldsymbol{k}_2}(t-t_0)} + \text{c.c.} \tag{S16}$$

When the system consists of a large (macroscopic) number of randomly place molecules, the self-heterodyne signal vanishes due to phase mismatching; in order to have a signal from a large number of molecules/systems, they should be organized in a periodic structure. In this case, since for an optical pump, the phase matching condition is automatically satisfied, we have

$$\langle\tilde{\sigma}_\mu(\boldsymbol{q},\tau)\rangle = \sum_{\boldsymbol{k}\in L_B}(2\pi)^3\delta(\boldsymbol{q}-\boldsymbol{k})\langle\tilde{\sigma}_s(\boldsymbol{k},\tau)\rangle, \tag{S17}$$

with $\hat{\sigma}_s(\boldsymbol{r})$ being the charge-density operator of the molecule/system, located at the center/origin of the periodic structure, while L_B is the the (Bragg) lattice, associated with our periodic structure the expression for the generalized signal adopts the form

$$\mathcal{S}(\boldsymbol{r},\boldsymbol{r}';t,t') = \frac{ie}{\hbar}\int_{t_0}^{t} d\tau \sum_{\boldsymbol{q}\in L_B}\frac{\langle\tilde{\sigma}_s(\boldsymbol{q},\tau)\rangle}{\boldsymbol{q}^2}\int_{\mathbb{R}^3}\frac{d\boldsymbol{k}_1}{(2\pi)^3}\int_{\mathbb{R}^3}\frac{d\boldsymbol{k}_2}{(2\pi)^3}\rho_{\boldsymbol{k}_1,\boldsymbol{k}_2}(t_0)e^{i[(\boldsymbol{k}_1+\boldsymbol{q})\cdot\boldsymbol{r}-\boldsymbol{k}_2\cdot\boldsymbol{r}']} \times e^{-i\varepsilon_{\boldsymbol{k}_1}(\tau-t_0)-i\varepsilon_{\boldsymbol{k}_1+\boldsymbol{q}}(t-\tau)+i\varepsilon_{\boldsymbol{k}_2}(t'-t_0)} + \text{c.c.} \tag{S18}$$

The interaction diagram of probing electron with the sample Coulomb potential formed in Eqs. (S16) and (S18) is depicted in Fig. S1.

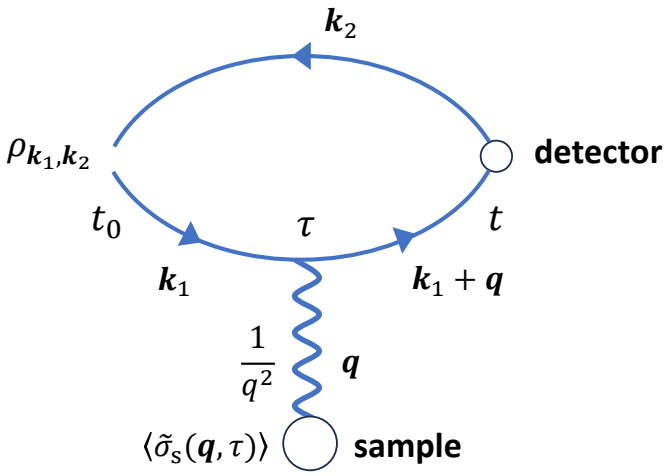

FIG. S1. Interaction diagram of self-heterodyned UED. Electron source eject electron, going through biprism and separate into two replica. After scattered with the sample at time τ, one replica changes its wave vector from $\mathbf{k}_1$ to $\mathbf{k}_1+\mathbf{q}$. The other replica has wave vector $\mathbf{k}_2$. Their trajectories are bent by applied magnetic field and gather at the detector at time t_D.

In this work, we do not study periodic system. We thus use the form of the correlation function Eq. (S16) for the following derivation.

The density matrix of the probe electron at time t is $\rho(\boldsymbol{r},\boldsymbol{r}';t) = \mathcal{S}(\boldsymbol{r},\boldsymbol{r}';t,t')|_{t'=t}$. Its corresponding electron current density at $\boldsymbol{r}$ is $\boldsymbol{j}(\boldsymbol{r},t) = -i\frac{\hbar}{2m}(\partial_{\boldsymbol{r}}-\partial_{\boldsymbol{r}'})\rho(\boldsymbol{r},\boldsymbol{r}',t)|_{\boldsymbol{r}'=\boldsymbol{r}}$. Then the detector measure the probe electron flux through a section of $\mathcal{A}$, $\int_{\mathcal{A}} d\boldsymbol{\zeta}\boldsymbol{n}(\boldsymbol{\zeta})\cdot\boldsymbol{j}(\boldsymbol{\zeta})$, where $\mathcal{A}$ is a surface embedded in $\mathbb{R}^3$, $\boldsymbol{\zeta}$ is a point on $\mathcal{A}$, $d\boldsymbol{\zeta}$ is the measure on $\mathcal{A}$, whereas $\boldsymbol{n}(\boldsymbol{\zeta})$ is the unit normal vector to $\mathcal{A}$ at $\boldsymbol{\zeta}$ in the direction of the flux. We introduce the fast/probe

electron flux function $f_{\mathcal{A}}$, associated with a surface/section $\mathcal{A}$ defined as a generalized function of two positions $\boldsymbol{r}$ and $\boldsymbol{r}'$

$$f_{\mathcal{A}}(\boldsymbol{r},\boldsymbol{r}') = -i\frac{\hbar}{2m}\delta'_{\mathcal{A}}\psi(\boldsymbol{r},\boldsymbol{r}'), \quad \int d\boldsymbol{r}d\boldsymbol{r}'\delta'_{\mathcal{A}}\psi(\boldsymbol{r},\boldsymbol{r}') = -\int_{\mathcal{A}} d\boldsymbol{\zeta}\boldsymbol{n}(\boldsymbol{\zeta})\cdot(\partial_{\boldsymbol{r}}-\partial_{\boldsymbol{r}'})\,\psi(\boldsymbol{r},\boldsymbol{r}')|_{\boldsymbol{r}=\boldsymbol{r}'=\boldsymbol{\zeta}}, \tag{S19}$$

and $\delta'_{\mathcal{A}}$ as a double-layer generalized function, associated with surface $\mathcal{A}$. The time-resolved electron counting signal is thus expressed in a simple and intuitive form

$$\mathcal{S}_0(\mathcal{A};t_D) = \int dt \int d\boldsymbol{r}d\boldsymbol{r}' g(t-t_D) f_{\mathcal{A}}(\boldsymbol{r},\boldsymbol{r}')\mathcal{S}(\boldsymbol{r},\boldsymbol{r}';t,t), \tag{S20}$$

where g is the detector entrance section and time gate function. The electron counting signals $\mathcal{S}_0$ is obtained upon the substitution of Eq. (S16) and Eq. (S19) into Eqs. (S20), which adopts the form

$$\mathcal{S}_0(\mathcal{A};\boldsymbol{q};t_D) = \frac{ie}{\hbar}\int_{t_0}^{\infty} d\tau \frac{\langle\tilde{\sigma}(\boldsymbol{q},\tau)\rangle}{\boldsymbol{q}^2} W_0(\mathcal{A};t_D,\boldsymbol{q},\tau) + \text{c.c.}, \tag{S21}$$

with the window function

$$\begin{aligned} W_0(\mathcal{A};t_D,\boldsymbol{q},\tau) = \frac{\hbar}{2m}\int_{\mathcal{A}} d\boldsymbol{\zeta}\int_{\mathbb{R}^3}\frac{d\boldsymbol{k}_1}{(2\pi)^3}\int_{\mathbb{R}^3}\frac{d\boldsymbol{k}_2}{(2\pi)^3}\rho_{\boldsymbol{k}_1,\boldsymbol{k}_2}(t_0)e^{i(\boldsymbol{k}_1+\boldsymbol{q}-\boldsymbol{k}_2)\cdot\boldsymbol{\zeta}}((\boldsymbol{k}_1+\boldsymbol{q}+\boldsymbol{k}_2)\cdot\boldsymbol{n}(\boldsymbol{\zeta})) \\ \times\int_{\tau}^{\infty} dt g(t-t_D)e^{-i\varepsilon_{\boldsymbol{k}_1}(\tau-t_0)-i\varepsilon_{\boldsymbol{k}_1+\boldsymbol{q}}(t-\tau)+i\varepsilon_{\boldsymbol{k}_2}(t-t_0)}. \end{aligned} \tag{S22}$$

Gate function g describes the temporal profile of the electron reaching the detector. For fast electron and a fixed sample-detector distance, the temporal gate function may be approximated as a δ-function. For periodic sample, S_0 in Eq. (S21) is a function of discrete value of $\boldsymbol{q}\in L_B$, where L_B is the periodic sample's corresponding Bragg's lattice.

It is convenient to express the probe electron single particle density matrix in terms of its counterpart, whose origin is located at the center of the electron Liouville space wavepacket at time t_0

$$\rho_f(\boldsymbol{r}_1,\boldsymbol{r}_2;t_0) = \tilde{\rho}_f(\boldsymbol{r}_1-\boldsymbol{r}_0,\boldsymbol{r}_2-\boldsymbol{r}_0;t_0), \quad \rho_{\boldsymbol{k}_1,\boldsymbol{k}_2}(t_0) = \tilde{\rho}_{\boldsymbol{k}_1,\boldsymbol{k}_2}(t_0)e^{i(\boldsymbol{k}_1-\boldsymbol{k}_2)\cdot\boldsymbol{r}_0}. \tag{S23}$$

If the setup includes a splitter that separates the heterodyne component of the electron pulse, e.g., to achieve the scattered and heterodyne electrons entering the detector, while moving in the same direction, a simple way to describe it is to use the following effective initial probe electron density matrix in a form

$$\rho_{\boldsymbol{k}_1,\boldsymbol{k}_2}(t_0) = \tilde{\rho}_{\boldsymbol{k}_1,S(\boldsymbol{k}_2)}(t_0)e^{i(\boldsymbol{k}_1\cdot\boldsymbol{r}_0-\boldsymbol{k}_2\cdot\boldsymbol{r}_h)}. \tag{S24}$$

with S being an SO(3) matrix that describes the rotation of the heterodyne component of the wavepacket.

S2. ANALYTICAL FORM OF THE WINDOW FUNCTION

As previously mentioned, the probing electron is described by a mixed state density matrix at time t_0. Instead of explicitly simulating the formation of the probing electron, as an approximation, we give the density matrix as a superposition of pure state density matrix with different center position at t_0 with a Gaussian weight factor. Each pure state is a Gaussian wave packet centered at $\mathbf{r}_0$ at reference time t_0 after being ejected from the source and before interacting with the sample. We assume the following electron wave function in real space at time t_0

$$\phi(r) = \frac{1}{\sqrt{2\pi}\sigma}e^{-i\boldsymbol{k}_0\cdot\boldsymbol{r}}e^{-\frac{(\boldsymbol{r}-\boldsymbol{r}_0)^2}{2\sigma^2}} \tag{S25}$$

where σ describe the spatial width of the electron at that time point. The corresponding wave function in k-space is

$$\phi_{\boldsymbol{k}_1} = 2\pi\sigma^2 e^{-\frac{\sigma^2}{2}(\boldsymbol{k}_0-\boldsymbol{k}_1)^2}e^{-2i(\boldsymbol{k}_0-\boldsymbol{k}_1)\cdot\boldsymbol{r}_0} \tag{S26}$$

For the mixed state, we assume the center of Gaussian wave packet $\boldsymbol{r}_0$ is centered around $\boldsymbol{R}$ and follows Gaussian distribution

$$\rho_{\boldsymbol{k}_1,\boldsymbol{k}_2} = \frac{1}{\sqrt{2\pi}\sigma_{\text{pulse}}}\int d\boldsymbol{r}_0 e^{-\frac{(\boldsymbol{r}_0-\boldsymbol{R})^2}{2\sigma^2_{\text{pulse}}}}\rho^{\text{pure}}_{\boldsymbol{k}_1,\boldsymbol{k}_2} = \frac{1}{\sqrt{2\pi}\sigma_{\text{pulse}}}4\pi^2\sigma^4\int d\boldsymbol{r}_0 e^{-\frac{(\boldsymbol{r}_0-\boldsymbol{R})^2}{2\sigma^2_{\text{pulse}}}}e^{-\frac{1}{2}\{\sigma^2[(\mathbf{k}_0-\mathbf{k}_1)^2+(\mathbf{k}_0-\mathbf{k}_2)^2]+2i(\mathbf{k}_1-\mathbf{k}_2)\cdot\mathbf{r}_0\}} \tag{S27}$$

where

$$\rho^{\text{pure}}_{\boldsymbol{k}_1,\boldsymbol{k}_2} = \phi_{\boldsymbol{k}_1}\phi^*_{\boldsymbol{k}_2} = 4\pi^2\sigma^4 e^{-\frac{1}{2}\{\sigma^2[(\mathbf{k}_0-\mathbf{k}_1)^2+(\mathbf{k}_0-\mathbf{k}_2)^2]+2i(\mathbf{k}_1-\mathbf{k}_2)\cdot\mathbf{r}_0\}}, \tag{S28}$$

σ_{pulse} is the variation of the $\boldsymbol{r}_0$ distribution of the electron pulse. Since $\sigma_{\text{pulse}}\gg\sigma$, we define pulse duration as $2\sigma_{\text{pulse}}/\boldsymbol{k}_0$.

S2.A. Window Function from Pure State Density Matrix

Substituting Eq. (S28) into Eq.(S22), performing Gaussian function integral of $\boldsymbol{k}_1, \boldsymbol{k}_2$, the window function corresponding to pure state density matrix can be written as

$$W_0^{\text{pure}}(\mathcal{A}; \boldsymbol{r}_0; t_D, \boldsymbol{q}, \tau) = \frac{\sigma^4}{2\pi}\frac{\hbar}{2m}\int_\tau^\infty dt\, g(t-t_D)\left(\frac{1}{\sqrt{\alpha_1\alpha_2}}\right)^3 \int_{\mathcal{A}} d\boldsymbol{\zeta}[\boldsymbol{q} - (\boldsymbol{\beta}_1 + \boldsymbol{\beta}_2)]\cdot \boldsymbol{n}(\boldsymbol{\zeta}) \exp\left(-\frac{1}{2}(\gamma_1+\gamma_2)\right) \tag{S29}$$

where

$$\alpha_1(t) = [\sigma^2 + i(t-t_0)], \qquad \alpha_2(t) = [\sigma^2 - i(t-t_0)] \tag{S30}$$

$$\boldsymbol{\beta}_1(\boldsymbol{q}, \boldsymbol{\zeta}, \tau, t) = \frac{-\sigma^2\boldsymbol{k}_0 - i\boldsymbol{\zeta} + i\boldsymbol{r}_0 + i(t-\tau)\boldsymbol{q}}{\sigma^2 + i(t-t_0)}, \qquad \boldsymbol{\beta}_2(t, \boldsymbol{\zeta}) = -\frac{\sigma^2\boldsymbol{k}_0 + i\boldsymbol{r}_0 - i\boldsymbol{\zeta}}{\sigma^2 - i(t-t_0)} \tag{S31}$$

$$\gamma_1(\boldsymbol{q}, \boldsymbol{\zeta}, \tau, t) = -\frac{[\sigma^2\boldsymbol{k}_0 + i\boldsymbol{\zeta} - i\boldsymbol{r}_0 - i(t-\tau)\boldsymbol{q}]^2}{\sigma^2 + i(t-t_0)} + \sigma^2\boldsymbol{k}_0^2 - 2i\boldsymbol{q}\cdot\boldsymbol{\zeta} + i(t-\tau)\boldsymbol{q}^2 \tag{S32}$$

and

$$\gamma_2(t, \boldsymbol{\zeta}) = -\frac{[\sigma^2\boldsymbol{k}_0 + i\boldsymbol{r}_0 - i\boldsymbol{\zeta}]^2}{\sigma^2 - i(t-t_0)} + \sigma^2\boldsymbol{k}_0^2 \tag{S33}$$

For simplicity, we choose the gate function of the detector to be $\delta-$function of time.

S2.B. Window Function from Mixed State Density Matrix

With mixed state density matrix Eq. (S27), the window function is

$$W_0(\mathcal{A}; t_D, \boldsymbol{q}, \tau) = \frac{1}{\sqrt{2\pi}\sigma_{\text{pure}}}\int d\boldsymbol{r}_0 e^{-\frac{(\boldsymbol{r}_0 - \boldsymbol{R})^2}{2\sigma_{\text{pulse}}^2}} W_0^{\text{pure}}(\mathcal{A}; \boldsymbol{r}_0; t_D, \boldsymbol{q}, \tau) \tag{S34}$$

Thus, we need to perform integration

$$I = \int d\boldsymbol{r}_0 e^{-\frac{(\boldsymbol{r}_0 - \boldsymbol{R})^2}{2\sigma_{\text{pulse}}^2}} (\boldsymbol{\beta}_1 + \boldsymbol{\beta}_2)\exp(-\frac{1}{2}(\gamma_1+\gamma_2)) \tag{S35}$$

We define

$$\boldsymbol{\eta}_1 = \sigma^2\boldsymbol{k}_0 + i\boldsymbol{\zeta} - i(t-\tau)\boldsymbol{q}, \qquad \boldsymbol{\eta}_2 = -\sigma^2\boldsymbol{k}_0 + i\boldsymbol{\zeta} \tag{S36}$$

the exponents in Eq. (S35) are collected as

$$\begin{aligned} &-\frac{1}{2}\left[\frac{(\boldsymbol{r}_0 - \boldsymbol{R})^2}{\sigma_{\text{pulse}}^2} - \frac{(\boldsymbol{\eta}_1 - i\boldsymbol{r}_0)^2}{\alpha_1} + \sigma^2\boldsymbol{k}_0^2 + i(t-\tau)\boldsymbol{q}^2 - 2i\boldsymbol{q}\cdot\boldsymbol{\zeta} - \frac{(i\boldsymbol{r}_0 - \boldsymbol{\eta}_2)^2}{\alpha_2} + \sigma^2\boldsymbol{k}_0^2\right] \\ =&-\frac{1}{2}\frac{\nu}{\mu}\left(\boldsymbol{r}_0 + i\frac{\Theta}{\nu}\right)^2 - \frac{1}{2}\frac{1}{\mu\nu}\Theta^2 - \frac{1}{2}\left(-\frac{\boldsymbol{\eta}_1^2}{\alpha_1} - \frac{1}{2}\frac{\boldsymbol{\eta}_2^2}{\alpha_2} + \frac{\boldsymbol{R}^2}{\sigma_{\text{pulse}}^2} + 2\sigma^2\boldsymbol{k}_0^2 + i(t-\tau)\boldsymbol{q}^2 - 2i\boldsymbol{q}\cdot\boldsymbol{\zeta}\right) \end{aligned} \tag{S37}$$

where we define

$$\mu = \alpha_1\alpha_2\sigma_{\text{pulse}}^2 \tag{S38}$$

$$\nu = \alpha_2\sigma_{\text{pulse}}^2 + \alpha_1\sigma_{\text{pulse}}^2 + \alpha_1\alpha_2 \tag{S39}$$

$$\Theta = \boldsymbol{\eta}_1\alpha_2\sigma_{\text{pulse}}^2 + \boldsymbol{\eta}_2\alpha_1\sigma_{\text{pulse}}^2 - \boldsymbol{q}\alpha_1\alpha_2\sigma_{\text{pulse}}^2 + i\boldsymbol{R}\alpha_1\alpha_2 \tag{S40}$$

The integral becomes

$$
\begin{aligned}
I =& \int d\boldsymbol{r}_0 \Big[\boldsymbol{q} - i\Big(\frac{1}{\alpha_1} - \frac{1}{\alpha_2}\Big)\boldsymbol{r}_0 + \frac{\boldsymbol{\eta}_1}{\alpha_1} - \frac{\boldsymbol{\eta}_2}{\alpha_2}\Big] \exp\Big[-\frac{1}{2}\frac{\nu}{\mu}\Big(\boldsymbol{r}_0 + i\frac{\Theta}{\nu}\Big)^2 - \frac{1}{2}\frac{1}{\mu\nu}\Theta^2 - \frac{1}{2}\Big(-\frac{\boldsymbol{\eta}_1^2}{\alpha_1} - \frac{\boldsymbol{\eta}_2^2}{\alpha_2} + \frac{\boldsymbol{R}^2}{\sigma_{\text{pulse}}^2} \\
&+ 2\sigma^2\boldsymbol{k}_0^2 + i(t-\tau)\boldsymbol{q}^2 - 2i\boldsymbol{q}\cdot\boldsymbol{\zeta}\Big)\Big] \\
=& \int d\boldsymbol{r}_0 \Big[\boldsymbol{q} - i\Big(\frac{1}{\alpha_1} - \frac{1}{\alpha_2}\Big)\Big(\boldsymbol{r}_0 + i\frac{\Theta}{\nu}\Big) + i\Big(\frac{1}{\alpha_1} - \frac{1}{\alpha_2}\Big)i\frac{\Theta}{\nu} + \frac{\boldsymbol{\eta}_1}{\alpha_1} - \frac{\boldsymbol{\eta}_2}{\alpha_2}\Big] \\
&\exp\Big[-\frac{1}{2}\frac{\nu}{\mu}\Big(\boldsymbol{r}_0 + i\frac{\Theta}{\nu}\Big)^2 - \frac{1}{2}\frac{1}{\mu\nu}\Theta^2 - \frac{1}{2}\Big(-\frac{\boldsymbol{\eta}_1^2}{\alpha_1} - \frac{\boldsymbol{\eta}_2^2}{\alpha_2} + \frac{\boldsymbol{R}^2}{\sigma_{\text{pulse}}^2} + 2\sigma^2\boldsymbol{k}_0^2 + i(t-\tau)\boldsymbol{q}^2 - 2i\boldsymbol{q}\cdot\boldsymbol{\zeta}\Big)\Big] \\
=& \int d\boldsymbol{r}_0 \Big[\boldsymbol{q} + i\Big(\frac{1}{\alpha_1} - \frac{1}{\alpha_2}\Big)i\frac{\Theta}{\nu} + \frac{\boldsymbol{\eta}_1}{\alpha_1} - \frac{\boldsymbol{\eta}_2}{\alpha_2}\Big] \exp\Big[-\frac{1}{2}\frac{\nu}{\mu}\Big(\boldsymbol{r}_0 + i\frac{\Theta}{\nu}\Big)^2 - \frac{1}{2}\frac{1}{\mu\nu}\Theta^2 - \frac{1}{2}\Big(-\frac{\boldsymbol{\eta}_1^2}{\alpha_1} - \frac{\boldsymbol{\eta}_2^2}{\alpha_2} + \frac{\boldsymbol{R}^2}{\sigma_{\text{pulse}}^2} \\
&+ 2\sigma^2\boldsymbol{k}_0^2 + i(t-\tau)\boldsymbol{q}^2 - 2i\boldsymbol{q}\cdot\boldsymbol{\zeta}\Big)\Big] \\
=& \Big[\boldsymbol{q} - \Big(\frac{1}{\alpha_1} - \frac{1}{\alpha_2}\Big)\frac{\Theta}{\nu} + \frac{\boldsymbol{\eta}_1}{\alpha_1} - \frac{\boldsymbol{\eta}_2}{\alpha_2}\Big] \exp\Big[-\frac{1}{2}\frac{1}{\mu\nu}\Theta^2 - \frac{1}{2}\Big(-\frac{\boldsymbol{\eta}_1^2}{\alpha_1} - \frac{\boldsymbol{\eta}_2^2}{\alpha_2} + \frac{\boldsymbol{R}^2}{\sigma_{\text{pulse}}^2} \\
&+ 2\sigma^2\boldsymbol{k}_0^2 + i(t-\tau)\boldsymbol{q}^2 - 2i\boldsymbol{q}\cdot\boldsymbol{\zeta}\Big)\Big]\sqrt{\frac{2\pi\mu}{\nu}}
\end{aligned}
\tag{S41}
$$

The window function becomes

$$
\begin{aligned}
W_0(\mathcal{A}; t_D, \boldsymbol{q}, \tau) =& \frac{\sigma^4}{2\pi}\frac{\hbar}{2m}\frac{1}{\sqrt{2\pi}\sigma_{\text{pulse}}}\int_\tau^\infty dt\, \delta(t - t_D)\Big(\frac{1}{\sqrt{\alpha_1\alpha_2}}\Big)^3 \Big[\boldsymbol{q} - \Big(\frac{1}{\alpha_1} - \frac{1}{\alpha_2}\Big)\frac{\Theta}{\nu} + \frac{\boldsymbol{\eta}_1}{\alpha_1} - \frac{\boldsymbol{\eta}_2}{\alpha_2}\Big] \\
&\exp\Big[-\frac{1}{2}\frac{1}{\mu\nu}\Theta^2 - \frac{1}{2}\Big(-\frac{\boldsymbol{\eta}_1^2}{\alpha_1} - \frac{\boldsymbol{\eta}_2^2}{\alpha_2} + \frac{\boldsymbol{R}^2}{\sigma_{\text{pulse}}^2} + 2\sigma^2\boldsymbol{k}_0^2 + i(t-\tau)\boldsymbol{q}^2 - 2i\boldsymbol{q}\cdot\boldsymbol{\zeta}\Big)\Big]\sqrt{\frac{2\pi\mu}{\nu}}
\end{aligned}
\tag{S42}
$$

S3. SIMULATION DETAILS

For Mg-phthalocyanine (Mg-Pc) molecule, the molecular geometry is optimized using DFT with the B3LYP functional[2–5] and the 6-31g(d) basis set and Gaussian 16[6]. The excited states are simulated by TDDFT calculations. Both valence and core excited states are computed with TDDFT in the Tamm-Dancoff approximation (TDA) using the Chronus Quantum software package[7]. The TDA calculations employ the same density functional and basis set used in the geometry optimization. For circularly polarized light (CPL) with circular polarization in x-y plane, the excited states of E_u irreducible representation with two-fold degeneracy in D_{4h} group are dipole allowed, and denoted mE_ux and mE_uy, where x, y denote the transition dipole direction, and $m, n = 1, 2..., 7$ is the index of pair of degenerate states. The excited states are listed in Tab. S1 in the supplementary information of Ref. [8].

We apply a circularly polarized pump pulse $\mathscr{E}_{\text{left}}(t) = E_0[\mathbf{e}_x \cos(\Omega(t)) - \mathbf{e}_y \sin(\Omega(t))] \exp\Big[-\frac{t^2}{2\tau_{\text{pu}}^2}\Big]$ propagating along z perpendicular to the molecular x-y plane with an amplitude of 6.9934×10^9 V/m, central frequency $\Omega = 4.0$ eV and $\tau_{\text{pu}} = 1.3$ fs at 0 fs to create the superposition of excited state. To include the entire pump pulse, we simulate the electronic dynamics from time -3.9 fs (-3 τ_{pu}) to 21.1 fs. The time evolution of ground state and excited state population is depicted in Fig. S2 in the supplementary information of Ref. [8].

S4. SIMULATION RESULTS

We depict the the charge migration dynamics with the real space charge density in Fig. S2. The snapshots of charge in q-space are given in Figs. S3 and S4, for real and imaginary part respectively. The time dependent heterodyne electron diffraction is depicted in Fig. S5. The time evolution of the diffraction pattern is in the video.

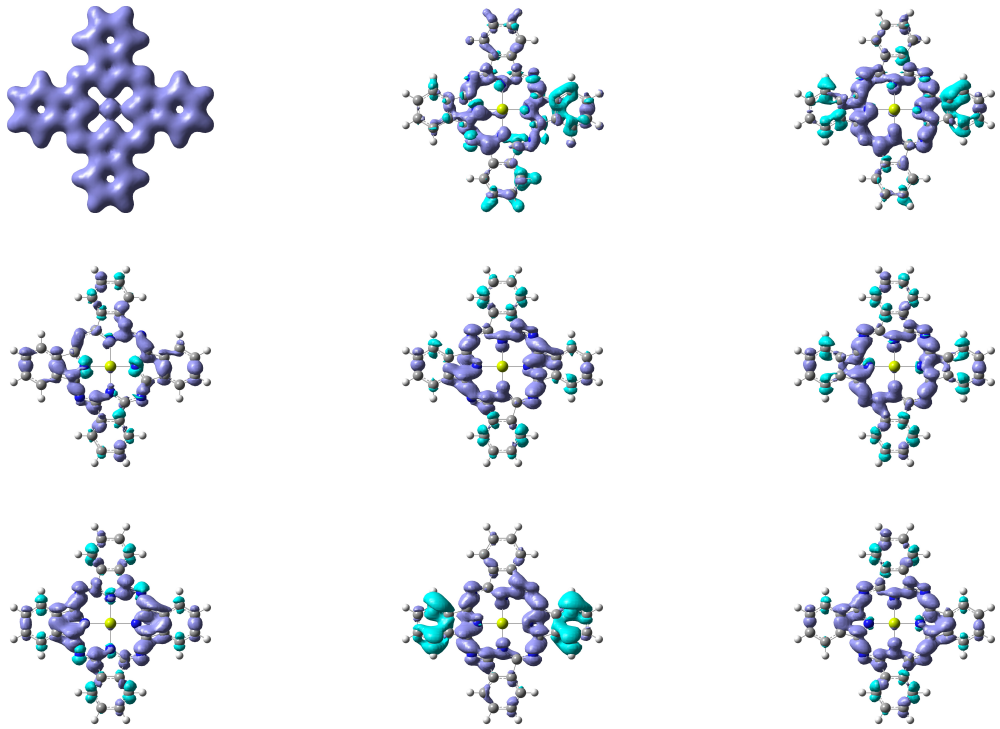

FIG. S2. Time evolution of molecular charge density in real space. The top left figure is the real space charge density $\sigma(\mathbf{r}, -3.7 \text{ fs})$. It is the ground state charge density, before the pump pulse. The following figures show the real space charge density difference $(\sigma(\mathbf{r}, \tau) - \sigma(\mathbf{r}, -3.7 \text{ fs}))$, where $\tau = -0.9$ fs, 2.1 fs, 5.1 fs, 8.1 fs, 11.1 fs, 14.1 fs, 17.1 fs, 20.1 fs respectively.

S5. COMPARISON WITH PINEM

The present self-heterodyne electron diffraction is different from an existing single electron pulse method known as Photon-Induced Near Field Electron Microscopy (PINEM) in the spatial resolution and the sample type[9–24]. In PINEM, a laser pulse excites a surface plasmon mode in a nanomaterial and an electron beam subsquently propagates through the sample and gains energy from the plasmon mode. The laser pulse transfers the photon energy to the electron through the molecular medium and the energy gain/loss spectrum of the electron due to inelastic scattering is finally measured. Since that spectrum is found to reach the maximum at the maximum temporal overlap of the optical and electron pulses, a combination of carefully overlapping laser and electron pulses together can be used as a probe in the PINEM. Similar to other electron microscopy methods, the nanoscale structure of the specimen can be measured by near-field imaging. The spatial resolution is determined by the focal point size of the probe pulse, which can be used for studying the structure of nanoaterial[13, 22, 24, 25] and biological specimens[26, 27]. In self-heterodyne electron diffraction, in contrast, there is a time delay between the laser and electron pulses resembling a pump probe technique. The single-electron pulse iteself serves as a scattering probe which can direclty image the structure of molecules with atomic spatial resolution, determined by the De Broglie wavelength.

[1] S. Mukamel, *Principles of Nonlinear Optical Spectroscopy* (Oxford University Press, 1995).
[2] A. D. Becke, Density-functional exchange-energy approximation with correct asymptotic behavior, Phys. Rev. A **38**, 3098 (1988).
[3] A. D. Becke, Density-functional thermochemistry. iii. the role of exact exchange, J. Chem. Phys. **98**, 5648 (1993).
[4] C. Lee, W. Yang, and R. G. Parr, Development of the colle-salvetti correlation-energy formula into a functional of the electron density, Phys. Rev. B **37**, 785 (1988).
[5] B. Miehlich, A. Savin, H. Stoll, and H. Preuss, Results obtained with the correlation energy density functionals of becke and lee, yang and parr, Chem. Phys. Lett. **157**, 200 (1989).

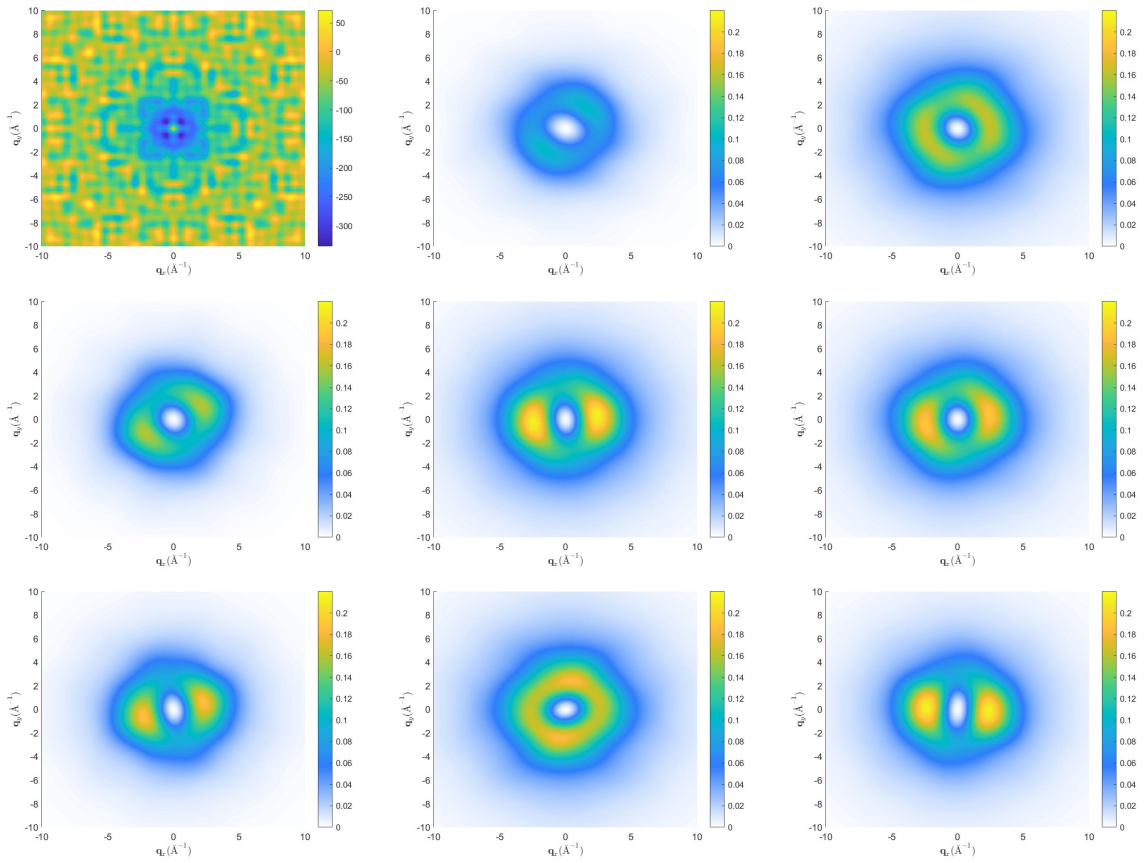

FIG. S3. Real part of the molecular charge density in q-space, where q_z is set to 0. The top left panel $\Re[\tilde{\sigma}(\mathbf{q}, -3.7 \text{ fs})]$ is the real part of ground state charge density in q-space. Its main contribution is the nuclear charge density. The following panels show the charge density difference where charge density at time delay τ subtract the initial charge density $\Re[\tilde{\sigma}(\mathbf{q}, \tau) - \tilde{\sigma}(\mathbf{q}, -3.7 \text{ fs})]$. The the time delay τ of the following figure are at -0.9 fs, 2.1 fs, 5.1 fs, 8.1 fs, 11.1 fs, 14.1 fs, 17.1 fs, 20.1 fs respectively.

[6] M. J. Frisch, G. W. Trucks, H. B. Schlegel, G. E. Scuseria, M. A. Robb, J. R. Cheeseman, G. Scalmani, V. Barone, G. A. Petersson, H. Nakatsuji, X. Li, M. Caricato, A. V. Marenich, J. Bloino, B. G. Janesko, R. Gomperts, B. Mennucci, H. P. Hratchian, J. V. Ortiz, A. F. Izmaylov, J. L. Sonnenberg, D. Williams-Young, F. Ding, F. Lipparini, F. Egidi, J. Goings, B. Peng, A. Petrone, T. Henderson, D. Ranasinghe, V. G. Zakrzewski, J. Gao, N. Rega, G. Zheng, W. Liang, M. Hada, M. Ehara, K. Toyota, R. Fukuda, J. Hasegawa, M. Ishida, T. Nakajima, Y. Honda, O. Kitao, H. Nakai, T. Vreven, K. Throssell, J. A. Montgomery, Jr., J. E. Peralta, F. Ogliaro, M. J. Bearpark, J. J. Heyd, E. N. Brothers, K. N. Kudin, V. N. Staroverov, T. A. Keith, R. Kobayashi, J. Normand, K. Raghavachari, A. P. Rendell, J. C. Burant, S. S. Iyengar, J. Tomasi, M. Cossi, J. M. Millam, M. Klene, C. Adamo, R. Cammi, J. W. Ochterski, R. L. Martin, K. Morokuma, O. Farkas, J. B. Foresman, and D. J. Fox, Gaussian 16 Revision A.03, gaussian Inc. Wallingford CT 2016.

[7] D. B. Williams-Young, A. Petrone, S. Sun, T. F. Stetina, P. Lestrange, C. E. Hoyer, D. R. Nascimento, L. Koulias, A. Wildman, J. Kasper, J. J. Goings, F. Ding, A. E. DePrince III, E. F. Valeev, and X. Li, The chronus quantum (chronusq) software package, WIREs Comput. Mol. Sci. **10**, e1436 (2020).

[8] S. Sun, H. Yong, F. Chen, and S. Mukamel, Coherent ring-current migration of mg-phthalocyanine probed by time-resolved x-ray circular dichroism, Chem. Sci. **13**, 10327 (2022).

[9] B. Barwick, D. J. Flannigan, and A. H. Zewail, Photon-induced near-field electron microscopy, Nature **462**, 902 (2009).

[10] L. Kasmi, D. Kreier, M. Bradler, E. Riedle, and P. Baum, Femtosecond single-electron pulses generated by two-photon photoemission close to the work function, New J. Phys. **17**, 033008 (2015).

[11] L. Waldecker, R. Bertoni, and R. Ernstorfer, Compact femtosecond electron diffractometer with 100 kev electron bunches approaching the single-electron pulse duration limit, J. Appl. Phys. **117** (2015).

[12] F. G. de Abajo and M. Kociak, Electron energy-gain spectroscopy, New J. Phys. **10**, 073035 (2008).

[13] F. J. García de Abajo, A. Asenjo-Garcia, and M. Kociak, Multiphoton absorption and emission by interaction of swift electrons with evanescent light fields, Nano Lett. **10**, 1859 (2010), https://doi.org/10.1021/nl100613s.

[14] A. Howie, Photon interactions for electron microscopy applications, **54**, 33502 (2011).

[15] M. Aidelsburger, F. O. Kirchner, F. Krausz, and P. Baum, Single-electron pulses for ultrafast diffraction, Proc. Natl. Acad. Sci. U.S.A. **107**, 19714 (2010).

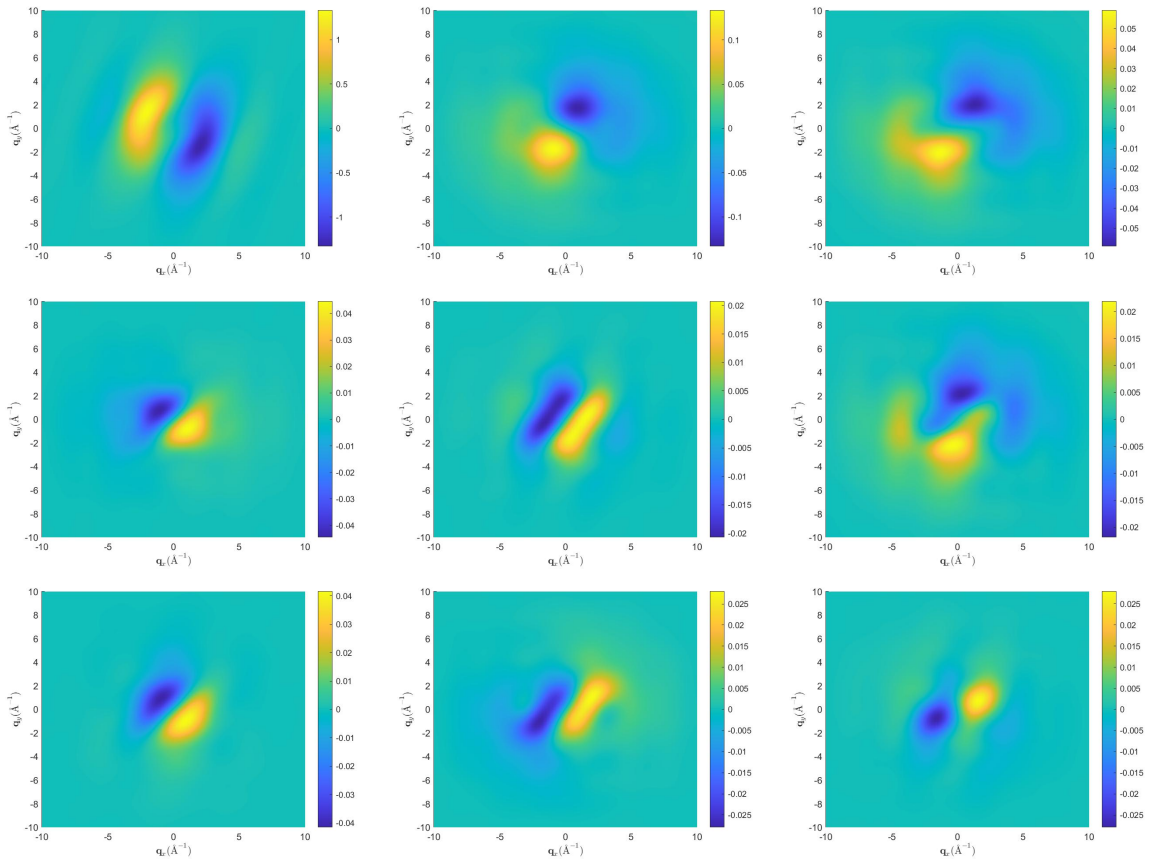

FIG. S4. Imaginary part of the molecular charge density in q-space. The top left panel is $\Im[\tilde{\sigma}(\mathbf{q}, -3.7 \text{ fs})]$, which is the imaginary part of ground state charge density in q-space. The following panels show the charge density difference where charge density at time delay τ subtract the initial charge density $\Im[\tilde{\sigma}(\mathbf{q}, \tau) - \tilde{\sigma}(\mathbf{q}, -3.7 \text{ fs})]$. The the time delay τ of the following figure are at -0.9 fs, 2.1 fs, 5.1 fs, 8.1 fs, 11.1 fs, 14.1 fs, 17.1 fs, 20.1 fs respectively.

[16] S. T. Park, M. Lin, and A. H. Zewail, Photon-induced near-field electron microscopy (pinem): theoretical and experimental, New J. Phys. **12**, 123028 (2010).

[17] S. T. Park and A. H. Zewail, Photon-induced near field electron microscopy, in *Ultrafast Imaging and Spectroscopy*, Vol. 8845, edited by Z. Liu, International Society for Optics and Photonics (SPIE, 2013) p. 884506.

[18] S. T. Park and A. H. Zewail, Photon-induced near-field electron microscopy: Mathematical formulation of the relation between the experimental observables and the optically driven charge density of nanoparticles, Phys. Rev. A **89**, 013851 (2014).

[19] S. T. Park and A. H. Zewail, Relativistic effects in photon-induced near field electron microscopy, J. Phys. Chem. A **116**, 11128 (2012), pMID: 22741915, https://doi.org/10.1021/jp304534n.

[20] M. T. Hassan, Attomicroscopy: from femtosecond to attosecond electron microscopy, J. Phys. B **51**, 032005 (2018).

[21] Y. Pan, B. Zhang, and A. Gover, Anomalous photon-induced near-field electron microscopy, Phys. Rev. Lett. **122**, 183204 (2019).

[22] K. Wang, R. Dahan, M. Shentcis, Y. Kauffmann, A. Ben Hayun, O. Reinhardt, S. Tsesses, and I. Kaminer, Coherent interaction between free electrons and a photonic cavity, Nature **582**, 50 (2020).

[23] O. Reinhardt and I. Kaminer, Theory of shaping electron wavepackets with light, ACS Photonics **7**, 2859 (2020), https://doi.org/10.1021/acsphotonics.0c01133.

[24] Y. Kurman, R. Dahan, H. H. Sheinfux, K. Wang, M. Yannai, Y. Adiv, O. Reinhardt, L. H. G. Tizei, S. Y. Woo, J. Li, J. H. Edgar, M. Kociak, F. H. L. Koppens, and I. Kaminer, Spatiotemporal imaging of 2d polariton wave packet dynamics using free electrons, Science **372**, 1181 (2021), https://www.science.org/doi/pdf/10.1126/science.abg9015.

[25] X. Fu, Z. Sun, S. Ji, F. Liu, M. Feng, B.-K. Yoo, and Y. Zhu, Nanoscale-femtosecond imaging of evanescent surface plasmons on silver film by photon-induced near-field electron microscopy, Nano Lett. **22**, 2009 (2022), pMID: 35226510, https://doi.org/10.1021/acs.nanolett.1c04774.

[26] D. J. Flannigan, B. Barwick, and A. H. Zewail, Biological imaging with 4d ultrafast electron microscopy, Proc. Natl. Acad. Sci. U.S.A. **107**, 9933 (2010).

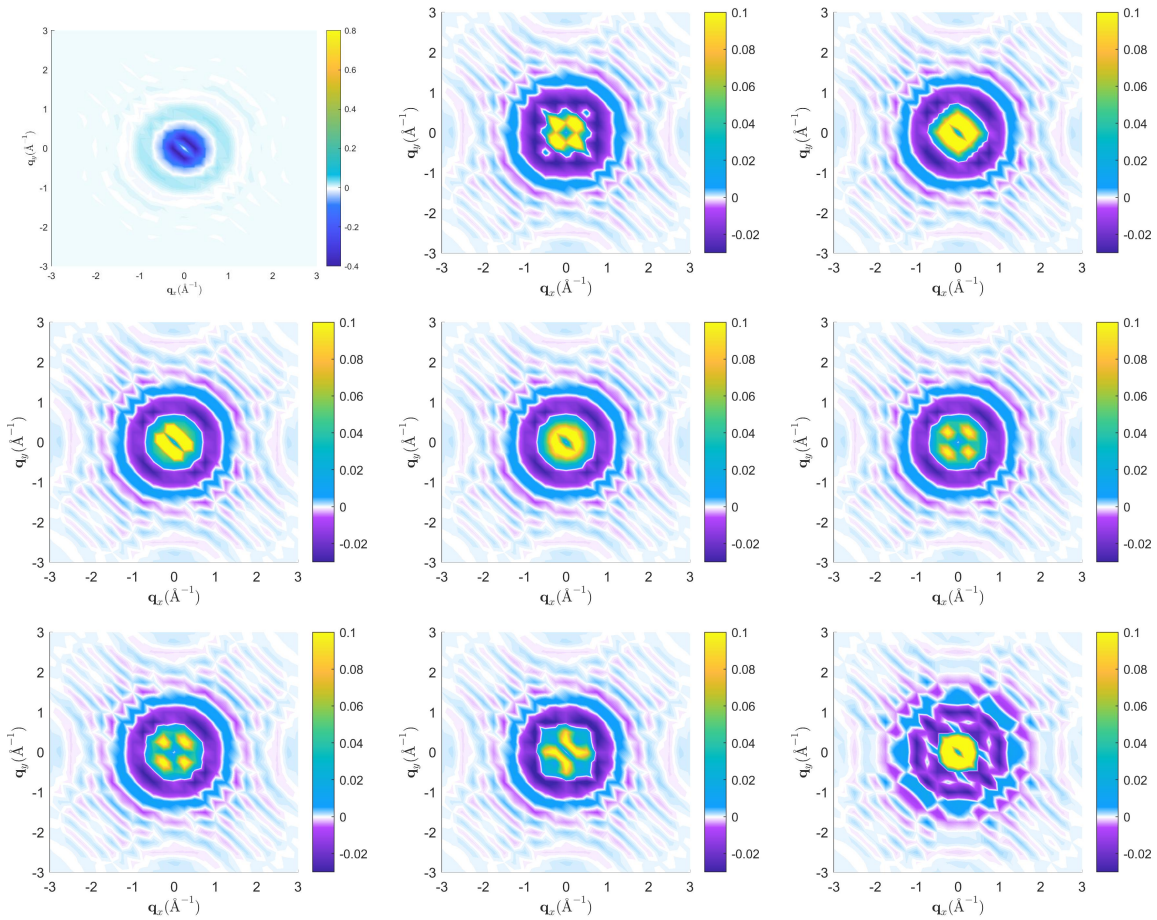

FIG. S5. Time dependent self-heterodyned ultrafast electron diffraction pattern of Mg-phthalocyanine. The top left panel shows the diffraction pattern before the pump pulse ($\mathcal{S}_0'(\mathbf{q}; -3.7 \text{ fs})$). The following panels show the diffraction signal at detection time t_D subtract the signal before the optical pump ($\mathcal{S}_0'(\mathbf{q}; t_D) - \mathcal{S}_0'(\mathbf{q}; -3.7 \text{ fs})$), where $t_D = -0.9$ fs, 2.1 fs, 5.1 fs, 8.1 fs, 11.1 fs, 14.1 fs, 17.1 fs, 20.1 fs respectively.

[27] M. Kaplan, B.-K. Yoo, J. Tang, T. E. Karam, B. Liao, D. Majumdar, D. Baltimore, G. J. Jensen, and A. H. Zewail, Photon-induced near-field electron microscopy of eukaryotic cells, Angew. Chem. **129**, 11656 (2017).